Generation of Linear Cluster States with a Deterministic Single Photon Source

THESIS

submitted in partial fulfillment of the
requirements for the degree of

MASTER OF SCIENCE
in
PHYSICS

Author :	Konstantin Iakovlev
Student ID :	s2109190
Supervisor :	Dr. Wolfgang Löffler
2^{nd} corrector :	Dr. Michiel de Dood

Leiden, The Netherlands, March 29, 2019

Generation of Linear Cluster States with a Deterministic Single Photon Source

Konstantin Iakovlev

Huygens-Kamerlingh Onnes Laboratory, Leiden University
P.O. Box 9500, 2300 RA Leiden, The Netherlands

March 29, 2019

Abstract

Cluster states are a viable resource for quantum computing where information is stored in these states and one single-qubit measurement is performed at a time. In order to generate such states, we use the quanta of light − photons − as our qubits. We generate them from a quantum dot in a microcavity which serves us as a deterministic single photon source. We explore a method of generating cluster states by entangling these photons with the means of linear optical elements and post-selection. We develop a theoretical model and show that it is in an agreement with our experimental data with single photons. From this agreement, we conclude that the cluster states arise in the experimental setup and the entanglement between the photons can be confirmed to be present with further analysis using our hypothesis and possibly even the quantum state tomography in the future.

Contents

Chapter 1

Introduction

Ever since the 1940s, the modern classical computers have been developing rapidly over the years after the revolutionizing "Universal Computing Machine" developed by Alan Turing. With ever so decreasing size of transistors, the physical limitations have already started showing an influence on computational systems. The transistors nearing the sizes within the atomic range can now fit into tiny computer chips in billions at a time. This introduces new boundaries to these shrinking system. The behaviour of electrons at such small sizes becomes peculiar and therefore the laws of quantum theory must be applied in order to resume the development of computational machines. In addition, the quantum aspects of information processing would increase the computational power exponentially. This motivates researchers to come up with new ways and methods of creating so-called quantum computer.

Quantum theory is, without a doubt, one of the most successful physical theories. It was developed in the beginning of the 20th century and succeeded at explaining many previously inexplicable physical phenomena and paradoxes which were incomprehensible with the use of classical theories [1].

The concept of a quantum computer would increase the computational power exponentially by using quantum properties to its advantage. Mainly, the concepts of quantum superposition and entanglement of qubits introduced by the quantum theory take the spotlight [2].

One possible resource for realisation of universal quantum computing are so-called cluster states [3]. Quantum information processing becomes possible when a sequence of single-qubit measurements is performed on these cluster states. In order to produce a useful quantum computing system, this realisation will require a controlled utilisation of likely thousands

of correlated qubits [4]. One scheme that is ideally suited for the cluster states is the so-called one-way quantum computing where information is implemented onto the cluster state and the measurements are performed on one qubit at a time [5]. In this model, the result of the measurement on a qubit always determines the basis of measurement on a following qubit and therefore the measurements are done on one qubit at a time. However, the successful realisation of the cluster states consisting of several qubits has turned out to be a difficult task [6,7].

In this thesis, we explore a new method of generating multi-photon cluster states with the use of deterministic single photon source − a quantum dot in a cavity. We use two types of excitation laser. A tunable continuous-wave laser and a coherent pulsed laser which generate a flow of single photons into a setup introduced by H. Eisenberg's research team in Racah Institute of Physics [3]. This setup entangles the photons into the cluster states. It is crucial that our photons are identical, i.e., indistinguishable from one another. We discuss different detection methods of detecting these states before evaluating their sustainability ourselves. We use mainly second order correlation measurements in order to characterize the states within our setup. We do this by post-selecting photons on various polarization states. Finally, we will analyse our results, present our conclusions and thoughts concerning the further development of the method. Positive results were obtained regarding the construction of predicted photonic states in our optical setup. However, elements of the imperfection were left mostly unconsidered which will require more work for future measurements. We hope that this research will lay the groundwork for the future experiments.

In this thesis, we will first discuss quantum mechanical concepts relevant for this project. With the help of these concepts we will explain the properties of our setup, single photon generation and the type of the cluster states which we expect to generate with our methods. Finally, we will present our results and the conclusion based on the analysis.

Chapter 2

Quantum Mechanical and Optical Concepts

In this chapter, various quantum mechanical along with quantum optical concepts and phenomena are introduced. We limit the number to only the concepts which are relevant to us in order to lay ground basis for this work.

2.1 Tensor product of Hilbert space $\mathcal{H}$

The general idea of a tensor product between two Hilbert spaces $\mathcal{H}_1, \mathcal{H}_2$ is that it creates another Hilbert space [8]

$$\mathcal{H} = \mathcal{H}_1 \otimes \mathcal{H}_2. \tag{2.1}$$

Before moving on, it is good to mark that the tensor product needs to satisfy the following linearity conditions

$$\Big(\mathbf{v} + \mathbf{w}\Big) \otimes \mathbf{u} = \mathbf{v} \otimes \mathbf{u} + \mathbf{w} \otimes \mathbf{u}, \tag{2.2}$$

$$\mathbf{u} \otimes \Big(\mathbf{v} + \mathbf{w}\Big) = \mathbf{u} \otimes \mathbf{v} + \mathbf{u} \otimes \mathbf{w}, \tag{2.3}$$

$$c\Big(\mathbf{v} \otimes \mathbf{u}\Big) = \Big(c\mathbf{v}\Big) \otimes \mathbf{u} = \mathbf{v} \otimes \Big(c\mathbf{u}\Big), \tag{2.4}$$

where $\mathbf{v}, \mathbf{w} \in \mathcal{H}_1$, $\mathbf{u} \in \mathcal{H}_2$ and $c \in \mathbb{C}$.

Now, consider the two Hilbert Spaces $\mathcal{H}_1, \mathcal{H}_2$ with bases $\{|i\rangle\}$, $\{|j\rangle\}$, respectively. This follows that the basis of the tensor product of the Hilbert spaces $\mathcal{H}_1 \otimes \mathcal{H}_2$ is $|i\rangle \otimes |j\rangle$.

If we want to create a combination of systems S in Hilbert space, we need to first consider a number n of separate systems which can be represented by state vectors $|S_n\rangle$ each of which belongs to a Hilbert Space $\mathcal{H}_{S_n}$. Now, the compound state S can be created by multiple tensor products between the Hilbert spaces. We assign a state vector to S and write it in the following form

$$|S\rangle = |S_1\rangle \otimes |S_2\rangle \otimes ... \otimes |S_n\rangle := |S_1, S_2, ..., S_n\rangle \tag{2.5}$$

2.2 Separability and Entanglement

Entanglement is an attribute of combined quantum systems [8]. In this section, the simplest case with two subsystems will be introduced, total of which is called bipartite system. First, we will discuss the bipartite systems before moving to tripartite systems which will be discussed briefly.

2.2.1 Bipartite system

Consider two quantum systems. The first system is constructed by Alice and the second one is constructed by Bob. Both systems belonging to Alice and Bob are described by vectors $|a\rangle$, $|b\rangle$ in $\mathcal{H}_1$ and $\mathcal{H}_2$, respectively. Their composite system is then a tensor product of the two Hilbert spaces $\mathcal{H} = \mathcal{H}_1 \otimes \mathcal{H}_2$. Now, any vector in composite space $\mathcal{H}$ can be written

$$|\psi\rangle = \sum_{i,j=1}^{d_1,d_2} c_{ij} |a_i\rangle \otimes |b_j\rangle , \tag{2.6}$$

where d_1, d_2 are the dimensions of $\mathcal{H}_1, \mathcal{H}_2$, respectively and c_{ij} are complex matrix elements.

Now we can define the entanglement for pure states.

Entanglement of pure states

Consider a pure state $|\psi\rangle \in \mathcal{H}$. It is called a *product state* or *separable* if it consists of states $|a\rangle \in \mathcal{H}_1$ and $|b\rangle \in \mathcal{H}_2$ such that

$$|\psi\rangle = |a\rangle \otimes |b\rangle , \tag{2.7}$$

holds. Otherwise the state $|\psi\rangle$ is *entangled* [9].

In physical sense, when a state is separable, the states of Alice and Bob are uncorrelated and the result Alice gets after a measurement will not depend on Bob's measurement outcome. Therefore, the product state can be prepared in a local way i.e. the state $|a\rangle$ is produced independently of the state $|b\rangle$. If, however, the states of Alice and Bob are in an entangled state, the states are then correlated and the outcome of Alice's measurement will determine the outcome of Bob's state. The entanglement can be explained in a way that if two different subsystems had interacted in the past, they can no longer be fully separate.

Schmidt Decomposition

If we consider a product state similar to the one depicted in equation (2.6), one can say that for each such state vector, there exist orthonormal bases $\{|\alpha_i\rangle\}_{d_1}$ of $\mathcal{H}_1$ and $\{|\beta_j\rangle\}_{d_2}$ of $\mathcal{H}_2$ such that

$$|\psi\rangle = \sum_{k=1}^{R} \sqrt{\lambda_k}\, |\alpha_k \beta_k\rangle \tag{2.8}$$

holds. Here, $R = \min\{d_1, d_2\}$ is called *Schmidt rank* and $\{\lambda_k\}_R$ is a set of decreasingly ordered non-negative numbers forming the *Schmidt vector* $\vec{\lambda_\psi}$ [8]. The vector $|\psi\rangle$ is entangled if and only if $R \geq 2$. Additionally R can be defined as the number of non-vanishing elements in the Schmidt vector $\vec{\lambda_\psi}$.

This theorem is a powerful tool in many calculations related to entanglement in bipartite systems. The proof of the theorem can be found in Ref. [8].

Entanglement of mixed states

In the majority of the cases, the states are various combinations of multiple pure states. These states are called mixed states and they are described by a density matrix which is a complex matrix

$$\rho = \sum_i p_i\, |\phi_i\rangle\, \langle\phi_i| \tag{2.9}$$

where $\sum_i p_i = 1, 0 \leq p_i \leq 1$ is some probability that the system is in a state $|\phi_i\rangle \in \mathcal{H}$.
The density matrix is positive semidefinite and hermitian. Additionally, followed from the normalization condition, to generally specify that ρ is a state, it has to fulfill $\mathrm{Tr}(\rho) = 1$. Continuing from the projection rule for

pure states [8], we can determine the pure state condition $\mathrm{Tr}(\rho^2) = 1$. All of this leads to a geometrical picture that the set of the states is a convex set. Convex set is a region in an Euclidean space where a line drawn between two elements of the set remains within the region, meaning that a convex combination of two states produces another state.

Now, we can finally define the entanglement for the mixed states. The principle is the same as in the entanglement for pure states. Consider states ρ_1 and ρ_2 which belong to Alice and Bob, respectively. Their composite system is then

$$\rho = \rho_1 \otimes \rho_2. \tag{2.10}$$

If there are probabilities p_i (convex weights [9]) and product states $\rho_{1_i} \otimes \rho_{2_i}$ such that

$$\rho = \sum_i p_i \Big(\rho_{1_i} \otimes \rho_{2_i} \Big), \tag{2.11}$$

holds, the state is separable. Otherwise, it is entangled.

Separability criteria

There are multiple criteria for both separability and entanglement but we will discuss only the criteria relevant to this work.

PPT and NPT criteria

Before we dive into the *partial transposition criterion*, we need to point out that any density matrix of a composite system can be expanded in a chosen product basis

$$\rho = \sum_{i,j}^{n} \sum_{k,l}^{m} p_{ij,kl} \left|i\right\rangle \left\langle j\right| \otimes \left|k\right\rangle \left\langle l\right|. \tag{2.12}$$

Now, we can define the partial transposition as transposition with respect to one subsystem of ρ. In this case we choose a transposition with respect to the subsystem of Alice

$$\rho^{T_A} = \sum_{i,j}^{n} \sum_{k,l}^{m} p_{ji,kl} \left|i\right\rangle \left\langle j\right| \otimes \left|k\right\rangle \left\langle l\right|. \tag{2.13}$$

Similarly, we can define the partial transposition with respect to Bob

$$\rho^{T_B} = \sum_{i,j}^{n} \sum_{k,l}^{m} p_{ij,lk} \left|i\right\rangle \left\langle j\right| \otimes \left|k\right\rangle \left\langle l\right|. \tag{2.14}$$

Version of March 29, 2019– Created March 29, 2019 - 13:57

The relations between partial and complete transposes for a density matrix of a bipartite system are

$$\rho^T = (\rho^{T_A})^{T_B} \Leftrightarrow \rho^{T_B} = (\rho^{T_A})^T \tag{2.15}$$

The spectrum of partial transposition does not depend on the product basis although the partial transposition in itself does [9]. The independence of the spectrum of the basis also holds for the full transposition.
If the partial transpose of a density matrix ρ does not have negative eigenvalues, we call the matrix ρ a PPT matrix or that it has *positive partial transpose*.
If the partial transpose of the matrix ρ has negative eigenvalues, it is called an NPT matrix (*negative partial transpose*).

Now, we can finally proceed to define PPT criterion [10].

PPT criterion

If ρ is a bipartite separable state, then it must be PPT.
This can be proven directly from the definition of separability in the equation (2.11). Both p_i and the product state $\rho_{1_i} \otimes \rho_{2_i}$ are positive, therefore also a partial transpose of the compose system has to be positive.

The criterion is very strong in terms of detecting an entanglement in a system as it states that if we calculate negative eigenvalues of the partial transpose of the system's density matrix ρ, it is a valid proof of an entanglement. However, PPT criterion is sufficient only for cases of 2x2 or 2x3 dimensions. This has been labeled as *Horodecki Theorem* and the proof can be found in Ref. [11].

In a simple way, the partial transpose can be thought of as time inversion of one element of a system. If a system of two particles is entangled and we reverse time of one of the particles, it violates the principle of positivity in quantum theory which is observed if negative eigenvalues are present in partial transpose of a density matrix.

Despite its flaws, the PPT criterion is the most popular criterion as it provides good characterization of the two qubit system [9]. Additionally, the amount of violation of the PPT criterion can quantify the entanglement [12].

2.2.2 Tripartite system

In this section we will discuss entanglement between three different parties. The concept of entanglement will be much broader than in bipartite

system mainly because several inequivalent classes of entanglement exist for systems with more than two parties. However, since we do not go beyond cases with three photons that will resemble our qubits in this work, we will limit ourselves to the tripartite systems.

Pure states

First, consider three separate qubit states $|\alpha\rangle$, $|\beta\rangle$ and $|\gamma\rangle$. Since two separate states can be composed into one party, there exist two kinds of separabilities.
Fully separable state is a state where all of the qubits are treated as separate systems and therefore written in the following way

$$|\psi\rangle_{A|B|C} = |\alpha\rangle_A \otimes |\beta\rangle_B \otimes |\gamma\rangle_C . \tag{2.16}$$

Like previously stated, we can compose two qubits into one state (for instance $|\delta\rangle_{AB} = |\alpha\rangle_A \otimes |\beta\rangle_B$) and as we are dealing with three different qubits, three different forms of *biseparable* states can be created

$$|\psi\rangle_{A|BC} = |\alpha\rangle_A \otimes |\delta\rangle_{BC} , \tag{2.17}$$

$$|\psi\rangle_{B|AC} = |\beta\rangle_B \otimes |\delta\rangle_{AC} , \tag{2.18}$$

$$|\psi\rangle_{C|AB} = |\gamma\rangle_A \otimes |\delta\rangle_{AB} . \tag{2.19}$$

For further notice, the composite state $|\delta\rangle$ is not guaranteed to be entangled state.

There also exists the third type of state called *genuine tripartite entangled state* which is neither of the previously mentioned states. Most important classes of the genuine tripartite entangled states are GHZ (Greenberger-Horne-Zeilinger) and W states:

$$|GHZ\rangle = \frac{|000\rangle + |111\rangle}{\sqrt{2}}, \tag{2.20}$$

$$|W\rangle = \frac{|100\rangle + |010\rangle + |001\rangle}{\sqrt{3}}. \tag{2.21}$$

It has been shown that a three party state $|\phi\rangle$ can be transformed into another three party state $|\psi\rangle$ with stochastic local operations and classical communication (SLOCC) [13]. This transformation is made possible with the help of three invertible operators A, B and C acting on the three qubit state

$$|\psi\rangle = A \otimes B \otimes C \, |\phi\rangle . \tag{2.22}$$

The invertibility feature of these operators tells us that the genuine entangled three-qubit states can be divided into different inequivalence classes which can not be further transformed by SLOCC. This creates two classes of tripartite entanglement, mainly GHZ and W classes. The reason why we distinguish these two classes is because W class states can be transformed via SLOCC into $|W\rangle$ state shown in equation (2.21) and the state $|GHZ\rangle$ in (2.20) represents the class of GHZ states.

From the generalization of Schmidt decomposition for three qubit system, with the help of local unitary operations, any pure three-qubit state can be transformed into

$$|\psi\rangle = \lambda_0 |000\rangle + \lambda_1 e^{i\theta} |100\rangle + \lambda_2 |101\rangle + \lambda_3 |110\rangle + \lambda_4 |111\rangle , \qquad (2.23)$$

where $\lambda_i \geq 0$, $\sum_i \lambda_i^2 = 1$, $\theta \in [0; \pi]$ [14].

It is good to mention that the W state is more durable than the GHZ state. In other words, if a particle is lost in GHZ state, it becomes a fully separable state but if one particle becomes detached in the W state, the state remains entangled. With this in mind, we can name the GHZ state maximally entangled state which is the best generalization of the Bell states and the W state is maximally entangled bipartite system in the reduced two-qubit states [9].

Mixed states

Definition of mixed states in tripartite systems is very similar to the one in the bipartite system. The mixed state of a tripartite system can be called fully separable if it can be written as a convex combination of separable pure states. With close resemblance to the mixed state in equation (2.9), we write

$$\rho^{fs} = \sum_i p_i |\phi_i^{fs}\rangle \langle \phi_i^{fs}| . \qquad (2.24)$$

If there are no such states and convex weights which would fulfill (2.24), the state is entangled.

Similarly, a biseparable state of three party system can be written as a convex combination of biseparable pure states

$$\rho^{bs} = \sum_i p_i |\phi_i^{bs}\rangle \langle \phi_i^{bs}| . \qquad (2.25)$$

Lastly, the mixed state can be fully entangled. In that case, it cannot be fully separable nor biseparable state. Just like in pure state, also in mixed states, there are two classes of fully entangled mixed states. Mixed

state is a part of GHZ class of states if it can not be written as a convex combination of W-type of pure states

$$\rho^W = \sum_i p_i \left|\phi_i^W\right\rangle \left\langle\phi_i^W\right| . \tag{2.26}$$

If the mixed state can be written in the form of (2.26), the state belongs to W class of states.

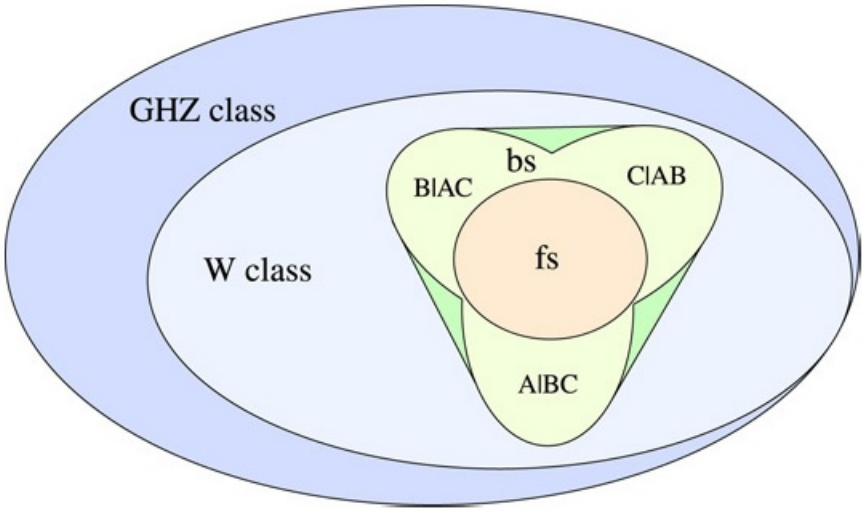

Figure 2.1: *Schematic representation of the sets of different mixed state classes. Figure is extracted from Ref. [9]*

Figure 2.1 shows that W class can be classified as a convex set within a convex set of GHZ class as it become GHZ state if the mixed state can not be written in the form of equation (2.26). A convex set made of fully separable states is a subset of possible biseparable states in (2.17)-(2.19). The biseparable states, on their hand, are a convex combination of biseparable states with respect to fixed partitions which are within a convex set of W class. All possible biseparable states are marked in green area. Note that three different forms of biseparable states in (2.17)-(2.19) do not make up the complete set of all biseparable states.

2.3 Hong-Ou-Mandel effect

In this section, we will discuss *Hong-Ou-Mandel* effect which is based on *quantum interference* of two indistinguishable photons. The effect is impor-

tant for this work as the photon indistinguishability M is of great importance for the successful generation of cluster states [15, 16].

Before proceeding to an example of such an effect, we will briefly discuss creation and annihilation operators.

Consider a simple *Fock state* or a *number state* $|n\rangle$ where n is the number of photons in that particular state. The applications of annihilation and creation operators on Fock states are as follows

$$\hat{a}\,|n\rangle = \sqrt{n}\,|n-1\rangle\,, \tag{2.27}$$

$$\hat{a}^\dagger\,|n\rangle = \sqrt{n+1}\,|n+1\rangle\,, \tag{2.28}$$

for all $n \geq 0$. Here, we see that the creation operator literally creates a photon and the annihilation operator destroys one. It is also good to know that the annihilation operator operating on a vacuum state $|0\rangle$ results in zero i.e. $\hat{a}\,|0\rangle = 0$.

Now we can proceed to a simple example of the Hong-Ou-Mandel effect. If we have two indistinguishable photons, a and b, arriving at a 1:1 beam splitter (Fig. 2.2) in different input modes 0 and 1, we can denote them as an input state $|1\rangle_0\,|1\rangle_1 = \hat{a}_0^\dagger \hat{a}_1^\dagger\,|0\rangle_0\,|0\rangle_1$. For a 1:1 beam splitter, the phase of transmitted and reflected beam differs by $\pi/2$ so we can write the relation between input and output modes of the beam splitter

$$\hat{a}_0^\dagger = \frac{1}{\sqrt{2}}(\hat{a}_2^\dagger + i\hat{a}_3^\dagger), \tag{2.29}$$

$$\hat{a}_1^\dagger = \frac{1}{\sqrt{2}}(i\hat{a}_2^\dagger + \hat{a}_3^\dagger). \tag{2.30}$$

Now we can write what happens in the beam slitter

$$\begin{aligned}
\hat{a}_0^\dagger \hat{a}_1^\dagger\,|0\rangle\,|0\rangle_{01} &\xrightarrow{BS} \frac{1}{2}(\hat{a}_2^\dagger + i\hat{a}_3^\dagger)(i\hat{a}_2^\dagger + \hat{a}_3^\dagger)\,|0\rangle\,|0\rangle_{23} \\
&= \frac{i}{2}(\hat{a}_2^{\dagger 2} + \hat{a}_3^{\dagger 2})\,|0\rangle\,|0\rangle_{23} \\
&= \frac{i}{\sqrt{2}}(|2\rangle\,|0\rangle_{23} + |0\rangle\,|2\rangle_{23}).
\end{aligned} \tag{2.31}$$

The final form of the output state was obtained with the help of equation (2.28). We see that the final output state shows bunching effect where both photons leave the beam splitter along one of the output modes, simultaneously. No case where two photons leave from different outputs emerges displaying the destructive two photon interference effect. For this to happen, the photons must be identical. Therefore, if the effect is practically observed, the photons can be defined as indistinguishable.

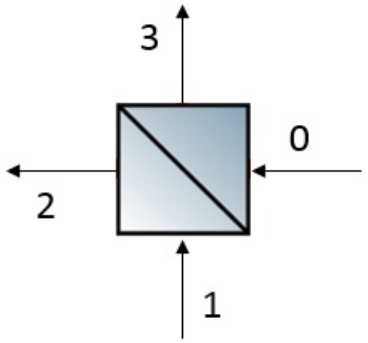

Figure 2.2: *1:1 beam splitter with two input and two output modes.*

2.4 Second order correlation

Just as indistinguishability, single photon purity i.e. antibunching of the photons determined by correlations is just as important for the success of generation of the cluster states [3, 17]. Correlation functions describe statistical and coherence properties of the electromagnetic fields. The degree of the coherence is correlation of the fields which is normalized and defines the characteristics of fluctuations between them. Since in this work only single photons will carry relevant weight for us, we will be discussing only second order i.e. $g^{(2)}$-correlation measurement which will be used to find statistical features between intensity fluctuations in our experiments.

Arguably the easiest way to observe and explain the single photon purity is by analyzing the second order correlation function $g^{(2)}(\Delta\tau)$ determined by a Hanbury-Brown-Twiss setup depicted in Figure 2.3. Assume an unknown light source i.e. we do not know whether photons arrive at the beam splitter of the setup individually or in bunched way. We only know that a group of photons arrive with a specific delay time $\Delta\tau$ due to a pulsed optical excitation. However, within that group the photons arrive at random time delays between them. At the beam splitter the photons are distributed into two different modes with equal probabilities before being detected by single photon avalanche photodetectors (SPAPDs) positioned at equal distances from the beam splitter. Detector A is connected to input port which starts the counter and detector B is connected to synchronizing port which stops the counter (Fig. 2.3). Subsequently, coincidence count is performed and the correlation function $g^{(2)}(\Delta\tau)$ is determined. If from the correlation function we observe an inequality for zero time delay such that $g^{(2)}(0) > g^{(2)}(\Delta\tau)$, we conclude that photons arrive in bunched man-

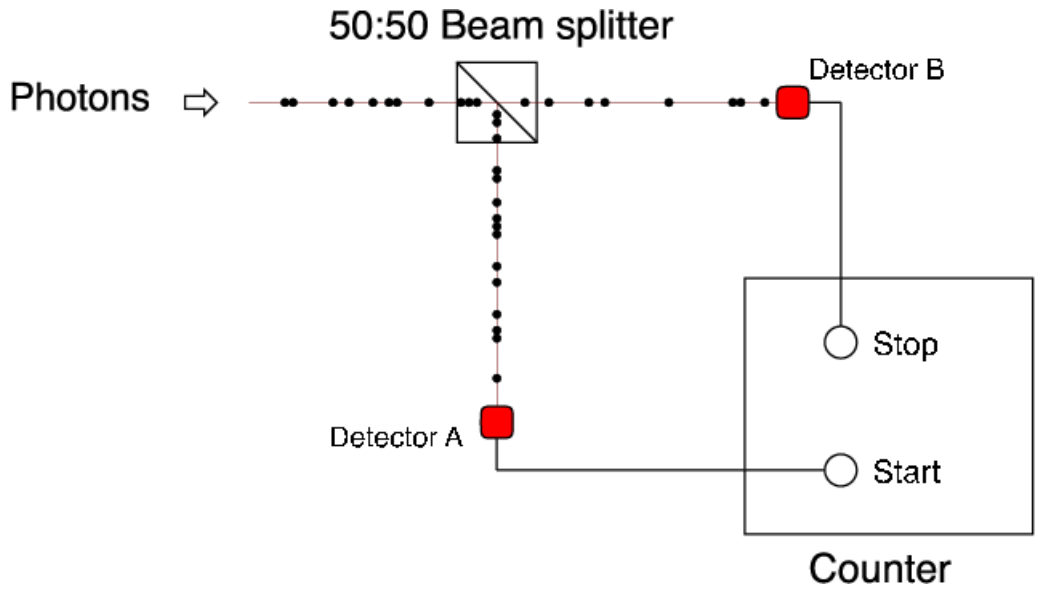

Figure 2.3: *Hanbury-Brown-Twiss setup typically used to measure $g^{(2)}$. If the photon is detected at Detector A a counter is started and it is stopped when another photon arrives at Detector B. Figure is extracted from Ref. [18]*

ner as two photons were detected simultaneously. On the other hand if we observe the function in such a way that $g^{(2)}(0) < g^{(2)}(\Delta\tau)$, we characterize the correlation as antibunching and can safely say that the source emits only single photons as no more than one detection was observed at a time. This is what we will strive for in this work. In the ideal case of antibunching $g^{(2)}(0) = 0$ but occasional deviations from it can be observed due to the background noise. Nonetheless as long as the background noise is small compared to a flow of single photons, these deviations should not carry much weight on our work.

Chapter 3

Linear Cluster States

Cluster states are a viable element of resource for the universal quantum computing where a sequence of single-qubit measurements is performed on a cluster state in order to accomplish coherent quantum information processing.

In this chapter, we will define general classes of cluster states, our setup that is capable of generating such states with multiple photons, and systematic procedure of the generation process of these states in the setup.

3.1 Cluster states

Cluster states, in quantum information, are a class of highly entangled states consisting of multiple qubits. Each of these prepared qubits is in a super-position state $\frac{1}{\sqrt{2}}(\,|0\rangle + |1\rangle\,)$, where $|0\rangle$ and $|1\rangle$ are a computational basis of the physical qubits [19]. More closely, a cluster state is a pure state of the qubits located on a cluster C which is a connected subset of a d-dimensional lattice where each qubit is connected with nearest-neighbour Ising type interactions [20]. These interactions can be triggered by different (entangling) correlation operators and can be described by an interaction Hamiltonian of the lattice model which generates a unitary transformation. This correlation operation usually takes the following form $|i\rangle\,|j\rangle \longrightarrow (-1)^{ij}\,|i\rangle\,|j\rangle$ where $i, j \in \{0, 1\}$. It is, then, applied between neighbouring qubits which cogently generates the entanglement between them.

In this work, we consider solely one dimensional cluster states in which case we consider a scenario of a chain of N qubits. More formally, if we denote our cluster state $|\Psi_N\rangle$, where N is number of qubits in a cluster C,

with nearest-neighbour interaction between neighbouring qubits, it can be written as

$$|\Psi_N\rangle = \frac{1}{2^{N/2}} \bigotimes_{a=1}^{N} \left(|0\rangle_a \, \sigma_z^{(a+1)} + |1\rangle_a \right), \tag{3.1}$$

where $a \in \mathbb{Z}^d$ are lattice sites, σ_z is a Pauli matrix and by convention $\sigma_z^{(N+1)} \equiv 1$. In cases for where $N = 2$ and $N = 3$, we can write the cluster state $|\Psi_N\rangle$ up to a local unitary transformation on the final qubit

$$|\Psi_2\rangle = \frac{1}{\sqrt{2}} \left(|0\rangle_1 |0\rangle_2 + |1\rangle_1 |1\rangle_2 \right), \tag{3.2}$$

$$|\Psi_3\rangle = \frac{1}{\sqrt{2}} \left(|0\rangle_1 |0\rangle_2 |0\rangle_3 + |1\rangle_1 |1\rangle_2 |1\rangle_3 \right), \tag{3.3}$$

respectively. $|\Psi_2\rangle$ corresponds to maximally entangled $|\phi^+\rangle$ Bell's state while $|\Psi_3\rangle$ corresponds to a GHZ state of three qubits which, in principle, is also fully entangled but not as robust as Bell's states.
However, with $N = 4$, the cluster state takes the following form

$$\begin{aligned} |\Psi_4\rangle = \frac{1}{2} \big(& |0\rangle_1 |0\rangle_2 |0\rangle_3 |0\rangle_4 + |0\rangle_1 |0\rangle_2 |1\rangle_3 |1\rangle_4 \\ & + |1\rangle_1 |1\rangle_2 |0\rangle_3 |0\rangle_4 - |1\rangle_1 |1\rangle_2 |1\rangle_3 |1\rangle_4 \big) \end{aligned} \tag{3.4}$$

which does not coincide with four-photon-GHZ state $|\mathrm{GHZ}_4\rangle$. In more general form, the cluster state $|\Psi_N\rangle$ and $|\mathrm{GHZ}_N\rangle$ are not equivalent for cases with $N > 3$. This means that these states cannot be transformed into one another with local operations and classical communication (LOCC). However, since in this work we will not go beyond the case with three qubits, we will not go into this issue in depth.

3.2 Setup

We introduce a new method of generating one dimensional multi-photon linear cluster states which uses quantum dot as a deterministic single photon source and linear optical elements for the means of entangling qubits i.e. photons in our setup. Additionally, in this work, we introduce two different ways to excite the quantum dot. Namely, these are a continuous-wave and a pulsed excitation lasers.

Quantum dots, as deterministic single photon sources, are much better than more conventional and more commonly used parametric down-conversion (PDC) sources. This is due to the probabilistic nature of PDC

where a typical probability of generating a photon pair is of only a few percent [3] while the quantum dots do not display probabilistic behaviour when producing single photons and therefore we can call them deterministic sources.

For simplicity, we will divide this section, required to understand the setup for generating linear cluster states, into three subsections:
1) Deterministic single photon source, i.e., a device with a quantum dot in it and an optical setup needed to generate a single photon stream
2) Generation and extraction of single photons where we explain step by step the process of generating single photons with our equipment
3) A setup with a delay-loop that generates linear cluster states with the means of linear optical elements and post selection.

3.2.1 Deterministic single photon source

Before we introduce the new generation scheme of cluster states that require separate qubit interacting with each other (in our work these qubit will be photons), we need a single photon source and as stated previously, in our case it is a sample with quantum dots.

The quantum dots are small sized semiconducting nanocrystals varying in diameter from one nanometer to a few dozen nanometers [21]. However, in this work, we use self-assembled InAs quantum dots of 2-3 nm in height and 10 nm in width. These quantum dots are able to confine positive and negative charges in three dimensions which is why energy states in quantum dots become quantized. This leads to charges and excitons showcasing the quantum mechanical features allowing discrete optical transitions to take place. For this reason, quantum dots are, sometimes, also called ”artificial atoms” [22]. In three dimensions, the movement of electrons is confined so tightly that the quantum dots excogitate zero dimensional bandstructure [23]. This leads the size of a quantum dot to directly control the properties of absorption and emission of energy. In this work, we consider the quantum dots to be simple two level systems consisting of a ground and an excited state.

In our setup, we use a closed-cycle exchange-gas vibration isolated cryostat where we keep a stable temperature of 7 K in order to minimize the effects of thermal fluctuations in the sample. At the bottom of the cryostat, a small muzzle or ”cold finger” is located where our sample is placed with two windows situated on each side of the muzzle. The sample contains a micropillar array of Fabry-Perot cavities (Fig. 3.1a and 3.1b) with quantum dots inside of them. The length of the cavities determine their

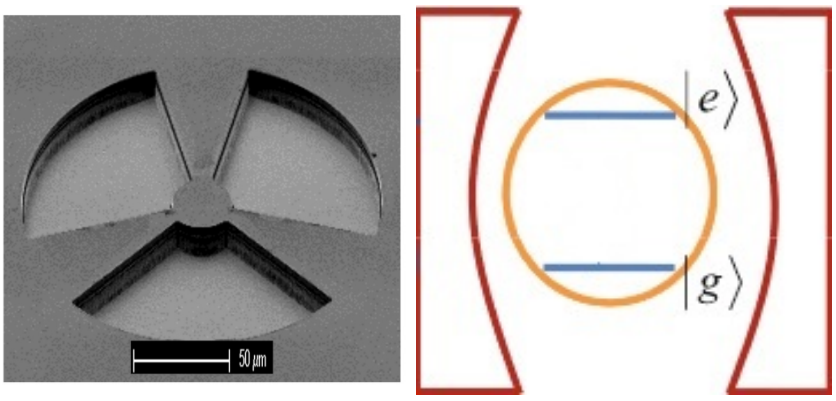

(a) **(b)**

Figure 3.1: *(a) Scanning electron microscope (SEM) image of oxide-aperture micropillar cavity [22]. (b) Fabry-Perot cavity with a QD inside displayed as two level system [24].*

resonance. On both ends of the array, several voltage contacts are attached so that a bias voltage can be applied. This voltage is, then, capable of tuning the Fermi level of the sample and therefore it can control the charge occupation of the quantum dot.

Both windows on the muzzle's sides allow application of transmission and reflection channels needed for aligning a tunable resonant scanning laser with the quantum dot, checking whether the laser is in resonance with the cavity and observing possible quantum dots coupled to a specific cavity mode. The reflection channel will play a much more significant role in our method than the transmission channel as the only utilization of the transmission channel will serve in the purpose of getting a scanning laser in resonance with the cavities.

The scanning laser we use is tunable (New Focus, Velocity, model 6319, 930-945nm, [22]), continuous-wave diode laser and we couple it to the cavity of our sample. Consequently, the dynamics of quantum dot exciton coupled to a cavity is described by the Jaynes-Cummings model. As a result, a spontaneous emission from the quantum dot takes place and the photon comes out of the cavity.

Fig. 3.2 demonstrates our setup where we use two different polarizers, two $\lambda/2$-half-waveplates, one $\lambda/4$-quarter-waveplate and a beam splitter. The $\lambda/2$-waveplate rotates the direction of the linearly polarized light while the $\lambda/4$-waveplate converts linearly polarized light into elliptically polarized light and other way around. This setup is used to generate a flow of single photons into the later-to-be-introduced setup that entangles

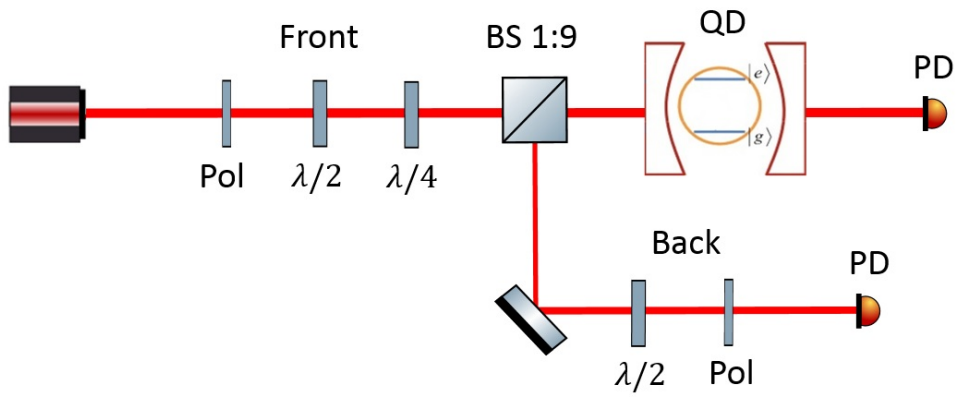

Figure 3.2: *Optical setup around the sample cavity with a quantum dot. Laser light is directed through a polarizer, a half-waveplate, a quarter-waveplate and a beam splitter before it reaches the Fabry-Perot cavity. Transmitted light is detected with a photodetector while reflected light is first rotated by another half-waveplate and a polarizer before being detected or directed to another setup wia single mode fiber.*

the single photons into cluster states. Before reaching the setup, the laser is first sent through a stack of filters in order to reduce its intensity and coupled to a single mode fiber which directs the laser light into the setup. It, then, travels through front polarizer, the front $\lambda/2$- and $\lambda/4$-waveplates, reaches the beam splitter with transmission-reflection ratio of 1:9 placed before the cavity with a purpose of reducing the intensity of light going into the sample, and propagates into the cavity. Subsequently, the reflected light from the cavity, is reflected off of the beam splitter in the direction of the back $\lambda/2$-waveplate and the back polarizer after which it is coupled to a single mode fiber directing the light into the second setup for generating cluster states. Both, the transmitted light through and the reflected light from the cavity can be coupled to photodetectors by the single mode fibers which allows monitoring of the intensities of light travelling in both channels.

The advantage of using single mode fibers is simple. They are better at retaining the fidelity of light over the long distances than the multi-mode fibers due to the their lower modal dispersion. For this reason alone, single mode fibers have a higher bandwidth than multi-mode fibers [26]. Nonetheless, we will be using both, the single mode and the multi-mode fibers in this work. Although, the fibers between the single photon source and the cluster state generation setup will be single mode fibers as quantum interference requires single spatial mode.

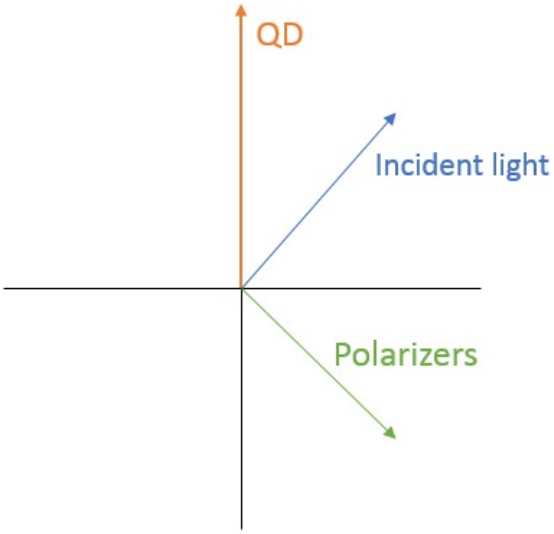

Figure 3.3: *Depiction of the ideal case of how the polarization of light and the back polarizer must be set (in relation to each other) in order to isolate single photons coming out of the quantum dot. The polarization of incident light is rotated away from the polarization of the quantum dot light and the back polarizer is set perpendicularly to incident light.*

The general idea of this setup comes from the fact that both, incident light we send in to excite the quantum dot and the single photon stream emitted by the dot come out of the cavity simultaneously into our reflection channel and we need to isolate the light coming out of the quantum dot so that we can utilize the single photons. The front polarizer, both $\lambda/2$- and front $\lambda/4$-waveplates are installed with a purpose of rotating the polarization of our incident light away from the polarization of the single photons coming out of the quantum dot, then we can set the back polarizer perpendicular to the polarization of the incident light in order to eliminate it completely while letting single photons pass further in the setup (Fig. 3.3).

3.2.2 Generation and extraction of single photons

In this section, we will explain step-by-step procedure of the excitation of the quantum dot and the isolation of the single photons emitted by the sample. The process will require multiple pieces of external equipment such as charge-coupled device (CCD)-camera, oscilloscopes, light-emitting diode (LED), avalanche photodetectors (APD) and LabVIEW soft-

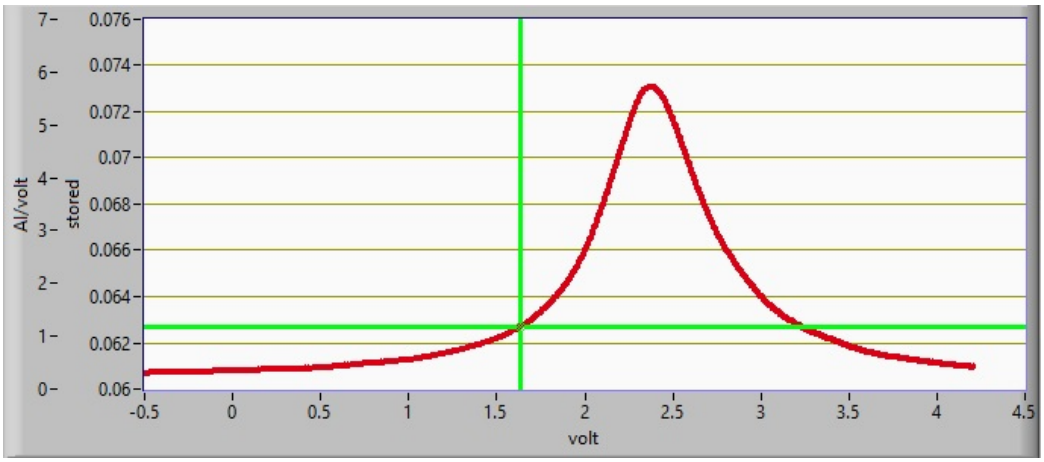

Figure 3.4: *A scan of transmitted laser light through the cavity displaying laser light to be resonant with the cavity at laser voltage of approximately 2.3 V. For this particular scan, the laser light was optimally aligned with the cavity and the wave-length of the laser was set to 934.2 nm.*

ware [27].

First, we choose a cavity in which we will probe the quantum dots. To do so, we send in LED light into our sample and inspect an array of oxide-aperture micropillar cavities. After choosing one cavity, we send in a laser light and with the help of the picture produced by the CCD-camera we align the laser light beam with the cavity by placing it in the middle of the cavity by moving the sample with variation of piezos on an XYZ-stage in three dimensions. Once the beam is in the middle, we turn off the LED light and on the oscilloscope inspect the intensity of the transmitted light through the cavity. In order to maximize the transmission, we first tune the laser to be resonant with the cavity by changing the laser wave-length while observing the oscilloscope. When we set the laser to a certain wave-length which generates a transmission curve in the oscilloscope (Fig. 3.4), we lock the laser to that wave-length and proceed to further optimize the transmission by realigning the sample with the piezos.

Once we are satisfied with the optimization of the transmission, we move on to inspect a reflected light directed into a single photon avalanche photodetector (SPAPD). We apply a stack of intensity filters of OD3 and OD1 before the front polarizer, due to the increased sensitivity of the detectors used in the reflection channel as the signal of the quantum dot is relatively weak compared to the intensity of the laser light. With displayed slow scan of intensity against the voltage of the scanning laser on LabVIEW software and by changing the bias voltage of the quantum dot, we

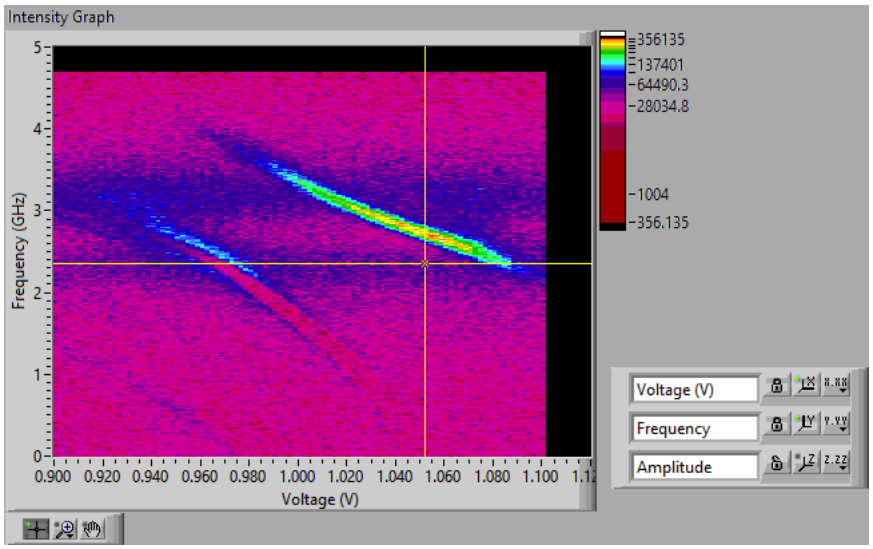

Figure 3.5: *Voltage against frequency scan where the increased photon count (line with bright colours) corresponds to the quantum dot inside the cavity with the corresponding bias voltage.*

are able to detect changes emerging in the reflection curve in the form of arising peaks which are determined to be the light coming from a quantum dot coupled to a cavity mode. In order to isolate this peak, we start one-by-one rotating the $\lambda/2$- and $\lambda/4$-waveplates to completely isolate the peak in question from the other light detected in the reflection channel. When the peak is sufficiently isolated from the rest of the light reflected off of the sample, we perform a bias voltage $-$ laser frequency scan (Fig. 3.5) where the increased colour contrast indicates the highest detected photon count rate over a range of bias voltages. We choose the best bias voltage based on the highest photon count rate on the graph produced by the scan and proceed back to the slow scan image of intensity against the laser voltage to further optimize the isolation of the peak of light coming from the quantum dot by rotating the waveplates. In Figure 3.6, we display an isolated quantum dot peak from the rest of the light reflected from the cavity. Ideally, there should be no other light detected other than that coming from the quantum dot which is not the case in our figure. However, the peak is sufficiently well isolated from the rest of the light for us to detect an adequate number of single photons against the count rate of the background noise coming from the exterior light sources in the lab and the leaked laser light reflected off the sample. However, the increase in the intensity at other values of the voltage is not entirely clear to us as we were not able to completely isolate the intensity peak but we suspect some kind of leak

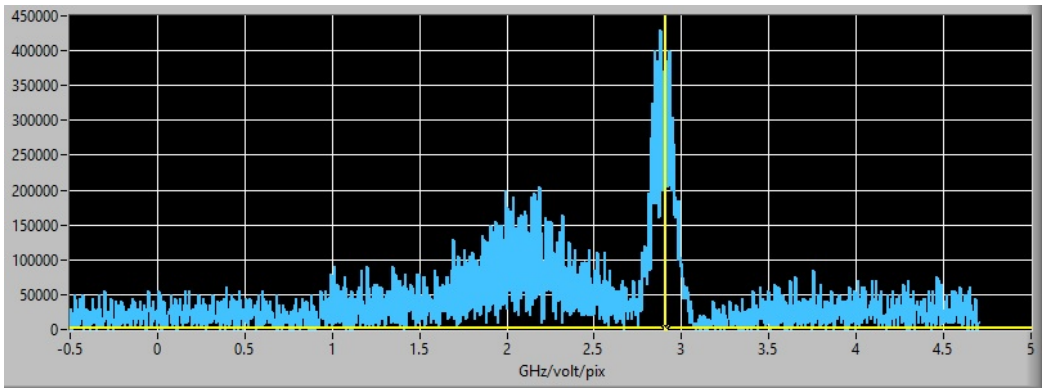

Figure 3.6: *Excitation laser frequency against the single photon count rate per second recorded by one APD. The peak of single photon intensity peak is clearly distinct from the rest of the registered photon counts. Rise in the photon count rate on the left side of the peak can be caused by a leak from another cavity mode. However, the peak from the quantum dot is relatively well isolated from the leaked light.*

from other cavity mode which, in principle, should not appear.

The voltage indicated at the location of the peak of intensity gives us the right direction for setting the right laser voltage to maximize the photon count rate of single photons. By varying this voltage, we can determine the maximum count rate of the photons going into an SPAPD per second and we leave the laser running at that specific voltage throughout our measurements.

Lastly, the light could be tested to be of origin of the quantum dot by simply changing the bias voltage of the quantum dot by a relatively high value which would result in a sudden drop of a single photon count rate going into an SPAPD indicating that most of the light was indeed coming from our quantum dot. This method could also be used to determine the background noises in the monitored single photon count. By blocking the reflection channel, we could determine that the background noise from the exterior light sources such as monitor screens, light leakage from other parts of the building and reflections off elements in the laboratory was approximately 1400 photon counts per second. By unblocking the reflection channel, and by changing the bias voltage enough to observe nearly zero light from the quantum dot, we determined that the total background noise, including the light from the exterior sources and the laser light, was approximately 60 000 counts against the total of 800 000 counts per second on average after the photons from the quantum dot were directed into the detectors again.

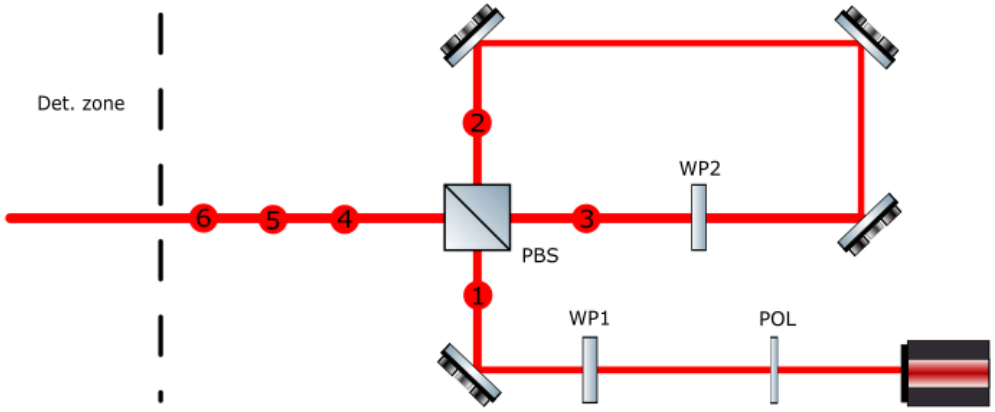

Figure 3.7: *The loop with time delay of 3.5 ns used for generating linear cluster states. Depicted are deterministic quantum dot source of single photons, polarizer, polarizing beam splitter and two half-wave plates both set at 22.5° in order to rotate polarization basis on Bloch sphere by 45°. Numbered circles indicate the locations in the setup relevant for understanding the generation process. The generated photonic state will subsequently be detected in the detection zone.*

In addition, the generation of single photons can be done, also, by using a pulsed laser in which case the photons would be directed into the reflection channels with intervals between them matching the time between the pulses of the excitation laser. For the purpose of the quality and the simpler understanding of our measurements, the pulsed laser is an ideal element for the excitation of the quantum dot. However, the generation of single photon flow using the pulsed laser holds its own challenges which will be discussed in the upcoming sections.

3.2.3 Setup for cluster state generation

After successfully generating and isolating the single photon stream coming from the quantum dot, we can direct the photons into the secondary setup pictured in Figure 3.7 which was first introduced by Y. Pilniyak [3]. The single photons arrive consecutively at the polarizing beam splitter with time differences between them depending on the method of excitation of the quantum dot. If the quantum dot is excited with continuous-wave laser, the photons will arrive at this setup in a tight chain where the time differences between the photons are largely random. If, however, the quantum dot is excited with a pulsed laser the photons will arrive with

time differences between them matching those between the pulses of the excitation laser.

The setup works in the following way. Photons arrive in the consecutive order at the polarizing beam splitter after passing through a polarizer and the first $\lambda/2$-waveplate (WP1) which is set to 22.5° in order to rotate the polarization of a photon by 45°. So, for instance, we set our polarizer so that it lets only H-polarized photons through. Consequently, the first waveplate rotates the photons into a superposition of $|H\rangle$ and $|V\rangle$ states. Our polarizing beam splitter operates on the traversing light so that the V-polarized component of the incident light is reflected and only the H-polarized component of light is transmitted into the loop. We also probed the polarization of the reflected light and the light going into the loop and discovered that while the transmitted light was purely H-polarized, approximately 1% of the reflected light was of undesired H-polarization. However, this small polarization error has little effect on our experiments. Inside the loop we have placed a second $\lambda/2$-waveplate (WP2) which is also set to 22.5 degrees to rotate the polarization of photons by 45°. The reason these waveplates are in the setup is that in order to entangle qubits into cluster states, the qubits must be found in superposition of the basis states, as mentioned in the beginning of this chapter where we explained what the cluster states are [3,20]. If we use the pulsed laser as our excitation method, the delay time introduced by the loop must be set to match the time difference between the pulses of the laser. The photons which are H-polarized are then transmitted through the polarizing beam splitter in the direction of the detection zone and photons with V-polarization are reflected back into the loop.

The entangling operation in this setup uses linear optical elements and post-selection. These optical elements are mainly the two waveplates before each input of the polarizing beam splitter and the polarizing beam splitter itself. Combining these elements with the post-selection produces an entanglement between photons corresponding to $|\Phi^+\rangle$ and $|\Phi^-\rangle$ Bell states [3]. Along with the entangled states we will examine the appearance of the quantum interference at the waveplates between the photons which we will demonstrate in the following section where the generation procedures of the photonic states between two and three different photons will be presented. These operations are unitary operations as long as they are not combined with post-selection. Nevertheless, since the polarization at the input ports of the polarizing beam splitter is well defined, the entangling operation should be the same whether the operations of the optical elements are combined with post-selection or not [3]. Furthermore, the quantum interference should, in principle, be nonlocal if the photons are

maximally indistinguishable [3].

The correlation measurements between the photons are then performed at the detection zone where we will use different configurations of APDs coupled to light by multi-mode fibers and polarizers set in front of the coupling fibers. We will introduce these configurations in the following section 3.3 where we will show the procedure of the generation of the photonic states in the setup with the loop.

3.3 Characterization of cluster states

Before we start displaying how the photonic states are generated in the setup for a variety of numbers of photons, we quickly remark that if we talk about the setup from now on, we will specifically refer to the setup with the loop introduced in section 3.2.3. The optical setup around the sample with the cavities in section 3.2.1 will not carry a relevant meaning for generation of the cluster states apart from being the deterministic single photon source for our work.

In this section, we will show how the photonic states with different numbers of photons can be generated in steps by operation rules of optical elements presented in the setup. We will discuss how these states appear in different parts of the setup, how they can be detected and measured and where the cluster states appear. In the first part of this section, we will examine the photonic state with two photons and in the second part three-photon states will be introduced.

In addition, unlike previously, we will be writing out the photonic states in $\{|H\rangle, |V\rangle\}$ basis instead of $\{|0\rangle, |1\rangle\}$ for the sake of simplicity because apart from the number of photons also their polarization, time and location will be relevant degrees of freedom. Furthermore, we will be using the following notation of the state

$$|P_l\rangle_t, \tag{3.5}$$

where P indicates polarization of the photon, the lower index t outside of the ket indicates time at which the state is observed and the lower index l inside the ket indicates the location of the photon in the setup at time t. Locations l will correspond to those illustrated in Figure 3.7. In addition, we remark that the time evolves by 3.5 ns, which is the delay time of the loop, only when the photon goes through the second half-wave plate (WP2) which is placed inside the loop. This time delay is precisely the time difference between the pulses of our pulsed excitation laser. We ne-

glect the time it takes for photons to travel in other parts of the setup as only the relative time difference between photons will be relevant.

Lastly, the operations of the waveplates at 22.5° on photons are written as

$$|H\rangle \xrightarrow{WP} \frac{1}{\sqrt{2}}\Big(|H\rangle + |V\rangle \Big) = |D\rangle\,, \tag{3.6}$$

$$|V\rangle \xrightarrow{WP} \frac{1}{\sqrt{2}}\Big(|H\rangle - |V\rangle \Big) = |A\rangle\,, \tag{3.7}$$

and the polarizing beam splitter transmits the H-polarized photons, while the V-polarized photons are reflected.

3.3.1 Two photons

We start by signing our photonic state with $|\Psi\rangle$, inserting one H-polarized photon into the setup at time $t = 0$ and by rotating it into a superposition at WP1. This produces our initial state

$$|\Psi\rangle = \frac{1}{\sqrt{2}}\Big(|H_1\rangle_0 + |V_1\rangle_0 \Big). \tag{3.8}$$

Subsequently, if a photon is transmitted into the loop, it is projected onto $|H\rangle$. If it is reflected, then it is in $|V\rangle$ state. Therefore, after the PBS, the state becomes

$$\xrightarrow{PBS} \frac{1}{\sqrt{2}}\Big(|H_2\rangle_0 + |V_4\rangle_0 \Big), \tag{3.9}$$

after which we have H-polarized photon inside the loop and WP2 rotates its polarization basis

$$\xrightarrow{WP2} \frac{1}{\sqrt{2}}\,|V_4\rangle_0 + \frac{1}{2}\Big(|H_3\rangle_{3.5} + |V_3\rangle_{3.5} \Big). \tag{3.10}$$

Now that our first photon has been evolved until $t = 3.5$ ns, we add a second H-polarized photon into our setup and rotate it at WP1

$$\longrightarrow \frac{1}{\sqrt{2}}\Big(|H_1\rangle_{3.5} + |V_1\rangle_{3.5} \Big) \otimes \left[\frac{1}{\sqrt{2}}\,|V_4\rangle_0 + \frac{1}{2}\Big(|H_3\rangle_{3.5} + |V_3\rangle_{3.5} \Big) \right]. \tag{3.11}$$

This is where the entangling operation takes place. In order to entangle two photons together, our first photon had to pass into the loop but the

polarization of the second photon is what determines whether the entangled state becomes $|\Phi^+\rangle$ or $|\Phi^-\rangle$ Bell state. Since the second photon we inserted was H-polarized, our photonic state takes the form

$$\xrightarrow{PBS} \frac{1}{2}\Big(|H_2\rangle_{3.5} + |V_4\rangle_{3.5}\Big)|V_4\rangle_0 + \frac{1}{2\sqrt{2}}\Big(|H_2H_4\rangle_{3.5,3.5} + |H_2V_2\rangle_{3.5,3.5} + |V_4H_4\rangle_{3.5,3.5} + |V_2V_4\rangle_{3.5,3.5}\Big) \tag{3.12}$$

where, for simplicity, we can express $|H\rangle \otimes |H\rangle \equiv |HH\rangle$ and the terms marked with red are the parts of the maximally entangled $|\Phi^+\rangle$ state equivalent to previously expressed two photon cluster state in equation (3.2). Henceforth, we can write the state in the following form

$$\frac{1}{2}\Big(|H_2\rangle_{3.5} + |V_4\rangle_{3.5}\Big)|V_4\rangle_0 + \frac{1}{2}|\Phi^+_{24}\rangle_{3.5} + \frac{1}{2\sqrt{2}}\Big(|H_2V_2\rangle_{3.5,3.5} + |V_4H_4\rangle_{3.5,3.5}\Big). \tag{3.13}$$

Now we may proceed to evolve our state until the time $t = 7$ ns

$$\xrightarrow{WP2} \frac{1}{2}\Big(\frac{1}{\sqrt{2}}\Big(|H_3\rangle_7 + |V_3\rangle_7\Big) + |V_4\rangle_{3.5}\Big)|V_4\rangle_0 + \frac{1}{2\sqrt{2}}\Big(\frac{1}{\sqrt{2}}\Big(|H_3\rangle_7 + |V_3\rangle_7\Big)|H_4\rangle_{3.5} + \frac{1}{\sqrt{2}}\Big(|H_3\rangle_7 - |V_3\rangle_7\Big)|V_4\rangle_{3.5}\Big) + \frac{1}{4}\Big(|H_3H_3\rangle_{7,7} - |V_3V_3\rangle_{7,7}\Big) + \frac{1}{2\sqrt{2}}|V_4H_4\rangle_{3.5,3.5}, \tag{3.14}$$

where the red parts indicate entangled photons and blue shows the product of the HOM-effect (section 2.3) which took place when an H- and a V-polarized photons arrived at WP2, simultaneously. With last PBS operation, we come to have our final state

$$\xrightarrow{PBS} \frac{1}{2\sqrt{2}}\Big(|H_4V_4\rangle_{7,0} + |V_2V_4\rangle_{7,0}\Big) + \frac{1}{2}|V_4V_4\rangle_{3.5,0} + \frac{1}{4}|H_4H_4\rangle_{7,3.5} + \frac{1}{4}|V_2H_4\rangle_{7,3.5} + \frac{1}{4}|H_4V_4\rangle_{7,3.5} - \frac{1}{4}|V_2V_4\rangle_{7,3.5} + \frac{1}{4}\Big(|H_4H_4\rangle_{7,7} - |V_2V_2\rangle_{7,7}\Big) + \frac{1}{2\sqrt{2}}|V_4H_4\rangle_{3.5,3.5}. \tag{3.15}$$

Here, we see that photons indicated to be in the location 4 have arrived at the detection zone at indicated to them times. Each term in this state

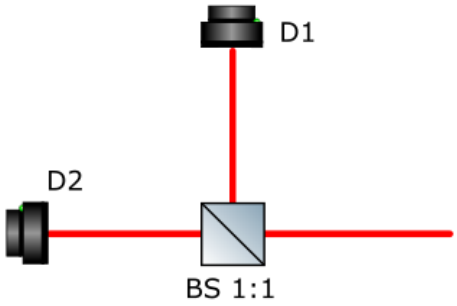

Figure 3.8: *Detection method for two photon states with 50/50 non-polarizing beam splitter set before the detectors.*

contains two photons and these terms are possible events which can be detected. The square of absolute value of the pre-factor of each term corresponds to the probability of the event to take place. We see that in occasional terms some photons are still left inside the loop at time $t = 7$ ns. However, we do not need to evolve the state any further as with each extra round inside the loop the time delay between the detectable photons grows by 3.5 ns while the probability of these detection events reduces exponentially with each taken round before they come out of the loop making them inconvenient for us from a practical point of view. This also indicates that there is always an extremely small probability that V-polarized component of light will be circulating inside the loop, indefinitely. However, in case the state must be developed further in time, the photons remaining inside the loop can be replaced by sums over the number of rounds in the loop

$$|V_2\rangle_t \longrightarrow \frac{1}{\sqrt{2}} \sum_{n=1}^{\infty} (-1)^{n-1} (\frac{1}{\sqrt{2}})^{n-1} |H_4\rangle_{t+3.5n} \,. \tag{3.16}$$

This sum corresponds to a possibility of the infinite time that light can remain circulating inside the loop. Here, n is the number of rounds the photon has been in the loop after entering it at time t. However, the use of this sum produces correct results only if it is applied to a term of the photonic state where one photon has already left the loop.

For the detection events, we have to use two single photon avalanche photodetectors (SPAPDs). The reason for having two detectors is their incapability of making two separate detections with time difference of 3.5 ns as their recovery time is approximately 60 ns. Therefore, in order to be able to record and gather relevant information we need to divide the output mode of the PBS going in the direction of the detection zone with a

non-polarizing beam splitter pictured in Figure 3.8 with 1:1 transmission-reflection ratio. This will reduce probabilities of certain events but since we will be mostly performing correlation measurements between two photons where only the quantitative ratios will be relevant, the reduction of these probabilities will not have serious impact on our measurements.

Measurements will be performed with different post-selective methods - mostly by one polarizer in front of each detector and by turning them to various configurations. For instance, the polarizer in front of the first detector could be set to H-polarization, while the polarizer before the other detector could be set to V-polarization and vice versa. This will allow us to post-select different groups of terms in our complete photonic state and see whether our predictions will hold.

One important aspect of detecting entanglement is performing measurements in two different bases which in our case will be $\{|H\rangle, |V\rangle\}$ and $\{|D\rangle, |A\rangle\}$ bases indicated in equations (3.6) and (3.7). To do so, we will place another $\lambda/2$-waveplate at 22.5 degrees in front of the non-polarizing beam splitter in order to rotate the polarization basis of each photon by 45 degrees before the beam splitter sends photons into the two detectors.

One important element that could be implemented in the setup is fast-speed modulator applied to the half-waveplate inside the loop. Its main enforcement would be the rotation of WP2 to 0° before the second photon inside the loop reaches it but not before the first photon would exit the loop in the direction of the detection zone. This would not only increase the probability of the detection events but also make the photobunching caused by the Hong-Ou-Mandel undetectable as it leaves the V-polarized photon of the pair trapped inside the loop indefinitely. However, during our work, these devices were not available and therefore not implemented into our setup.

3.3.2 Three photons

In order to advance from two photon cluster states to the states with three photons, we need to develop our state until the point in time when the first photon of the entangled pair is outside of the loop while the second one is still inside of it (equation (3.14)) and add the third H-polarized photon into our setup and rotate it at WP1 so that the state in the setup becomes

$$\frac{1}{\sqrt{2}}\Big(|H_1\rangle_7 + |V_1\rangle_7\Big) \otimes \left[\frac{1}{2}\Big(\frac{1}{\sqrt{2}}\Big(|H_3\rangle_7 + |V_3\rangle_7\Big) + |V_4\rangle_{3.5}\Big)\,|V_4\rangle_0\right.$$

$$+\frac{1}{2\sqrt{2}}\Big(\frac{1}{\sqrt{2}}\Big(|H_3\rangle_7+|V_3\rangle_7\Big)|H_4\rangle_{3.5}+\frac{1}{\sqrt{2}}\Big(|H_3\rangle_7-|V_3\rangle_7\Big)|V_4\rangle_{3.5}\Big)$$
$$+\frac{1}{4}\Big(|H_3H_3\rangle_{7,7}-|V_3V_3\rangle_{7,7}\Big)+\frac{1}{2\sqrt{2}}|V_4H_4\rangle_{3.5,3.5}\Big], \tag{3.17}$$

where in the first row we see that we are combining the first two photons with the additional third photon.

Next, the photons travel through the polarizing beam splitter after which we will start making out the potential entangled three photon state in the form of the GHZ state for three photons

$$\xrightarrow{PBS}\frac{1}{4}\Big(|H_2H_4V_4\rangle_{7,7,0}+|H_2V_2V_4\rangle_{7,7,0}+|V_4H_4V_4\rangle_{7,7,0}+|V_4V_2V_4\rangle_{7,7,0}\Big)$$
$$+\frac{1}{2\sqrt{2}}\Big(|H_2V_4V_4\rangle_{7,3.5,0}+|V_4V_4V_4\rangle_{7,3.5,0}\Big)$$
$$+\frac{1}{4\sqrt{2}}\Big(|H_2H_4H_4\rangle_{7,7,3.5}+|H_2V_2H_4\rangle_{7,7,3.5}+|V_4H_4H_4\rangle_{7,7,3.5}+|V_4V_2H_4\rangle_{7,7,3.5}$$
$$+|H_2H_4V_4\rangle_{7,7,3.5}-|H_2V_2V_4\rangle_{7,7,3.5}+|V_4H_4V_4\rangle_{7,7,3.5}-|V_4V_2V_4\rangle_{7,7,3.5}\Big)$$
$$+\frac{1}{4\sqrt{2}}\Big(|H_2H_4H_4\rangle_{7,7,7}-|H_2V_2V_2\rangle_{7,7,7}+|V_4H_4H_4\rangle_{7,7,7}-|V_4V_2V_2\rangle_{7,7,7}\Big)$$
$$+\frac{1}{4}|H_2V_4H_4\rangle_{7,3.5,3.5}+\frac{1}{4}|V_4V_4H_4\rangle_{7,3.5,3.5}, \tag{3.18}$$

where the elements of the GHZ state for the three photons are highlighted with red colour, while the last one of the three photons is still inside the loop indicating that a detection of this entangled state would require its isolation from other possible detection events in the setup and detection of each of the photons every period of 3.5 ns. Since only one of the previously entangled photons arrives at the PBS simultaneously with the third photon, the entanglement is formed only between the second and the third photon while entanglement between the first and the second photons still prevails. Hence, one dimensional cluster states.

Now that the focus of all the possible detection events (red part) has been established, we can write out the whole photonic state after another PBS transformation applied to the state

$$\xrightarrow{WP2,PBS}\frac{1}{4\sqrt{2}}|H_4H_4V_4\rangle_{10.5,7,0}+\frac{1}{4\sqrt{2}}|V_2H_4V_4\rangle_{10.5,7,0}+\frac{1}{4}|V_4H_4V_4\rangle_{7,7,0}$$

$$
\begin{aligned}
&+\frac{1}{8}\Big(|H_4H_4V_4\rangle_{10.5,10.5,0}-|H_4V_2V_4\rangle_{10.5,10.5,0}+|V_2H_4V_4\rangle_{10.5,10.5,0}-|V_2V_2V_4\rangle_{10.5,10.5,0}\Big)\\
&+\frac{1}{4\sqrt{2}}\Big(|V_4H_4V_4\rangle_{7,10.5,0}-|V_4V_2V_4\rangle_{7,10.5,0}\Big)\\
&+\frac{1}{4}\Big(|H_4V_4V_4\rangle_{10.5,3.5,0}+|V_2V_4V_4\rangle_{10.5,3.5,0}\Big)+\frac{1}{2\sqrt{2}}|V_4V_4V_4\rangle_{7,3.5,0}\\
&+\frac{1}{8}\Big(|H_4H_4H_4\rangle_{10.5,7,3.5}+|V_2H_4H_4\rangle_{10.5,7,3.5}-|V_4H_4V_4\rangle_{7,10.5,3.5}+|V_4V_2V_4\rangle_{7,10.5,3.5}\Big)\\
&+\frac{1}{8}\Big(|H_4H_4H_4\rangle_{10.5,10.5,3.5}-|V_2V_2H_4\rangle_{10.5,10.5,3.5}\Big)\\
&+\frac{1}{4\sqrt{2}}|V_4H_4H_4\rangle_{7,7,3.5}+\frac{1}{8}\Big(|V_4H_4H_4\rangle_{7,10.5,3.5}-|V_4V_2H_4\rangle_{7,10.5,3.5}\Big)\\
&+\frac{1}{8}\Big(|H_4H_4V_4\rangle_{10.5,7,3.5}+|V_2H_4V_4\rangle_{10.5,7,3.5}\Big)\\
&-\frac{1}{8}\Big(|H_4H_4V_4\rangle_{10.5,10.5,3.5}-|V_2V_2V_4\rangle_{10.5,10.5,3.5}\Big)+\frac{1}{4\sqrt{2}}|V_4H_4V_4\rangle_{7,7,3.5}\\
&+\frac{1}{8}\Big(|H_4H_4H_4\rangle_{10.5,7,7}+|V_2H_4H_4\rangle_{10.5,7,7}\Big)\\
&-\frac{1}{8\sqrt{2}}\Big(|H_4H_4H_4\rangle_{10.5,10.5,10.5}-|H_4H_4V_2\rangle_{10.5,10.5,10.5}\\
&-|V_2V_2H_4\rangle_{10.5,10.5,10.5}+|V_2V_2V_2\rangle_{10.5,10.5,10.5}\Big)\\
&+\frac{1}{4\sqrt{2}}|V_4H_4H_4\rangle_{7,7,7}\\
&-\frac{1}{8\sqrt{2}}\Big(|V_4H_4H_4\rangle_{7,10.5,10.5}-2\,|V_4V_2H_4\rangle_{7,10.5,10.5}+|V_4V_2V_2\rangle_{7,10.5,10.5}\Big)\\
&+\frac{1}{4\sqrt{2}}\Big(|H_4V_4H_4\rangle_{10.5,3.5,3.5}+|V_2V_4H_4\rangle_{10.5,3.5,3.5}\Big)+\frac{1}{4}|V_4V_4H_4\rangle_{7,3.5,3.5}\,.
\end{aligned}
\tag{3.19}
$$

It is vital to know that although post-selection seems to be an easy way out in characterization of such a long state, it is crucial for us to explicitly write out every single event in the setup because due to the limitations imposed by our detection methods, we are required to perform second order correlation measurements in order to observe the possible events. To be able to draw any conclusions concerning entanglement, we will need

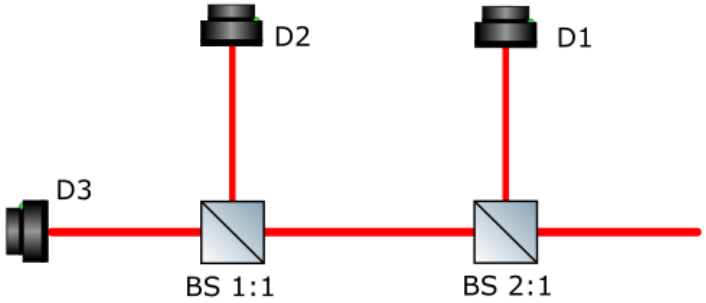

Figure 3.9: *Setup for detecting three photon states with beam splitters set in such way that each photon would have equal probability of* 33.3% *of reaching each detector.*

to consider every single possibility happening within the built setup and the detection equipment.

The detections will be made in the same manner as in the case with two photons. Only this time we will need three avalanche photodetectors (APDs) due to their frail recovery time of approximately 60 ns. However, while increasing the number of detectors, we need to maintain the ratio between the probabilities of the detection events. We can do this, by introducing two separate beam splitters with different transmission-reflection ratios. Figure 3.9 illustrates the detection zone for the three photon states. First, we divide the light path into two modes with a beam splitter whose transmission-reflection ratio is 2:1 where the reflected light goes directly into the first detector while the transmitted photons pass through another beam splitter with equal probabilities of transmitting and reflecting the light. The properties of these two beam splitters and the order that they are placed in ensure that each photon coming out of the loop will have equal probability of 33.3% being detected at each detector which guarantees the preservation of ratios between the detection probabilities and features in required correlation measurements.

Chapter 4

Experimental realisation

When it comes to the experiments, the most important and arguably the most difficult aspect of the optical setup is the strict precision at which optical elements must be aligned with respect to one another. Their location, distance and respective angle to the propagating light must be optimized to increase the functionality of the setup.

In this chapter, we will discuss some of the constructional and technical aspects of our setup, characterization of the setup using the continuous-wave and pulsed lasers, and lastly the correlation measurements that confirm the generation of a two-photon cluster state.

4.1 Setup preparation

Figure 4.1 displays the experimental setup used for generation of the cluster states as it was used in the laboratory with an addition of the optical elements forming a detection zone for the measurements of the states with two single photons. The loop, where the generation of the cluster states must take place, is constructed with a polarizing beam splitter. Each of the input modes has a half-waveplate turned to 22.5° which rotates the polarization of the photons by 45°. Before the loop, the front polarizer makes sure the entering photons are of H-polarized nature. After the photons are either reflected off or transmitted through the polarizing beam splitter in the direction of the detection zone, they propagate to another beam splitter which is non-polarizing with 1:1 transmission-reflection ratio. This beam splitter splits the photons into two modes A and B which eventually will travel to both photodetectors at the end of the modes. The photodetectors are coupled to the incoming light by multi-mode fibers which are differ-

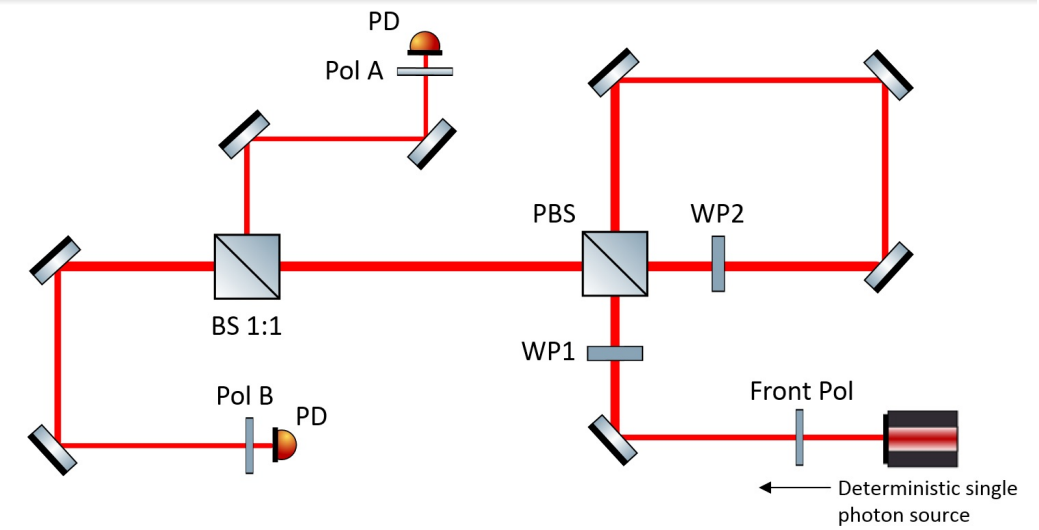

Figure 4.1: *Experimental setup used for detection of two photon states. The Front Polarizer is set so that only the H-polarized photons are sifted into the setup, the two half-waveplates in front of each input port of the polarizing beam splitter are set to 22.5° and the beam splitter has 1:1 transmission-reflection ratio. Photons are recorded by photodetectors before which two different polarizers are set.*

ent in length by several meters. However, before being detected by the photodetectors, the photons first travel through the post-selecting polarizers A and B, which we can set in any arbitrary angle in order to select a particular detection polarization. The single-photon detectors are connected to TimeHarp 260 PicoQuant^{TM} correlation card which will record time-differences between coinciding photons detected by the two detectors, where temporal order is preserved. Expressly, the photodetector connected to the input port is behind polarizer A and the synchronizing port is behind the polarizer B.

One of the more important aspects of the setup is aligning two beams going into the non-polarizing beam splitter in the detection zone. These beams are those reflected off and transmitted through the polarizing beam splitter. This serves not only in purpose of generated entanglement but also the quantum interference that must take place at WP2. There are two maneuvers that have to be performed in order to optimize and secure the best possible the alignment.

First, if the loop is misaligned, we need to take into account that each of the two beams coming out from the output mode of the PBS is split into two at the non-polarizing beam splitter resulting in 4 total beams beyond it. In order to make sure that all of these beams are aligned, we need to

record them simultaneously with a two-dimensional intensity profile captured by a beam profiler. If we were to record all the beams after the BS, we would see that tweaking one of the mirrors inside the loop would result in two split beams moving in different directions in two dimensional space. So, in order to align the beams, we need to record both modes after the BS simultaneously, while aligning two mirrors of the loop at the same time. We do this by first directing continuous-wave laser through our setup and placing the camera into the transmitted BS mode close to the polarizer. Next, we set a flip mirror to the other mode in such way that it reflects the beams from this mode into the camera. This forms four recorded intensity profiles. Now, by aligning the two mirrors within the loop, we align four beams into two Gaussian intensity profiles in the recording camera which guarantees the alignment between the beams.

Secondly, we place the camera before the BS and a polarizer set to 45° in front of the camera. We record the intensity profiles of the two beams coming from the PBS. If they form one Gaussian field without fringes, we can say that they are aligned. Additionally, the whole intensity oscillates due to unavoidable air turbulence.

These two steps were performed several times within the setup with positive results of Gaussian profiles emerging in the recorded intensity profile, ensuring that the light travelling into the loop was aligned with the light reflected off of the PBS.

Furthermore, the following statistical aspects of the setup were probed. The polarizing beam splitter was transmitting purely H-polarized light while the reflected light was 99% V-polarized. The losses within the loop were observed to be approximately 7% most likely due to imperfect anti-reflection coatings on the optical elements. The distance of the loop was approximately 1.05 m obtain the time delay of 3.5 ns, matching a two-pulse excitation scheme. The non-polarizing BS was characterized to transmit 49% and reflect 47% of light. The coupling between light and the multi-mode fibers was at 81% and 95% for the detectors A and B, respectively. Polarizers A and B were also observed to absorb approximately 15% and 5% of the light, respectively.

4.2 Testing the setup with pulsed laser

After the alignment of our setup, we sent in double-pulses of light from a coherent pulsed laser with a delay time of 3.5 ns between them while the two pulses were repeated every 12.5 ns. We recorded these pulses with one chosen APD (mode B after the beam splitter) without a polarizer in

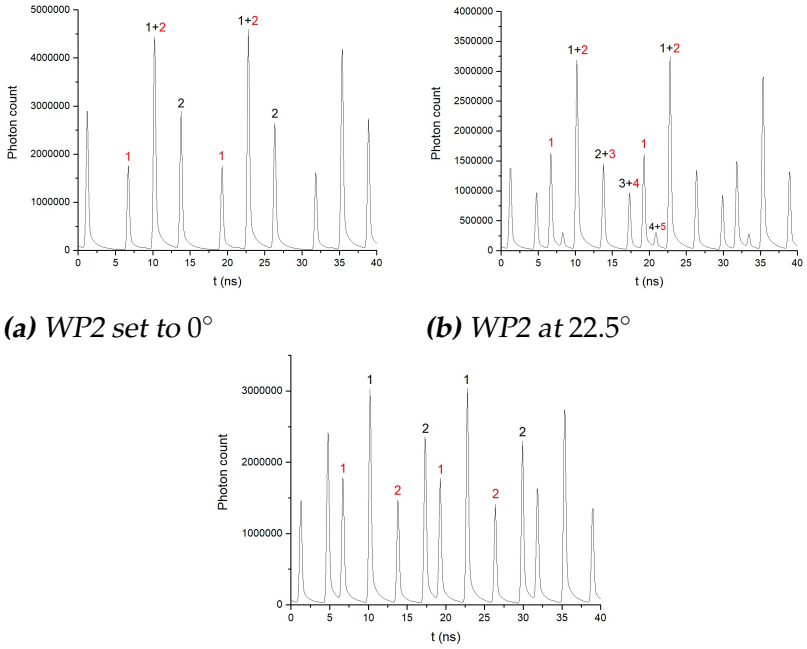

(a) *WP2 set to* 0°

(b) *WP2 at* 22.5°

(c) *WP2 at* 45°

Figure 4.2: *Recorded two pulses of light travelling through the setup with time difference of* 3.5 *ns. Peak marked with red are of the first pulse and with black of the second pulse. Peaks with the number one are detected elements of light that were reflected from the PBS never ending up inside the loop. Peaks indicated with other numbers correspond to the light transmitted into the loop and the increasing numbers to the number of rounds light stayed inside the loop.*

front of it. The photon counts were recorded in three different configurations − WP2 set to 0°, 22.5° and 45°. The recorded photon counts in these configurations are displayed in Figure 4.2a, b and c, respectively.

With WP2 set to 0°, the pulse traversing through the loop has to come out after 3.5 ns leaving no light inside the loop. This is what we also observe in Figure. 4.2a. Half of the light of the first pulse (1) is reflected from the PBS while the second part (2) comes out of the loop 3.5 ns later without traces of light left in the loop. Similar behaviour was observed in the second pulse. Now, we also see the second part of the first pulse and the first part of the second pulse (1+2) add up confirming that the delay times between the pulses and the loop indeed match. The relative size of the peaks (1), (1+2) and (2) shows that 50% of light was transmitted into the loop.

When WP2 is set to 22.5° (Fig. 4.2b), we must observe half of the ingoing light inside the loop as being reflected back in after each round. Our

experiment gives precisely that result with a drop of 50% in intensity of the detected light at every 3.5 ns. Overlapping of the parts of the two pulses are also observed in the similar way as in the previous experiment.

Lastly, WP2 is set to 45° (Fig. 4.2c). Our expectation is that the pulses, again, must be split in half at the PBS and the part going into the loop must stay inside the loop two rounds before being transmitted out without leaving any light behind. This is due to the fact that during the first round inside the loop light is rotated to V-polarization resulting in full reflection back into the loop and another rotation at WP2, then, sets it to H-polarization which is transmitted out. This is precisely what we observe in our measurement with no observed overlapping between the pulses due to the time differences of the detections. This measurement also shows that the two pulses were not of equal intensity and that the loss of 7% inside the loop was indeed present which can be seen in the height difference of the peaks 1 and 2. The latter conclusion was made due to the lack of overlapping between the two pulses which made the relative height of the peaks more distinct.

The measurement results show us that the setup works as planned, splitting in-going light in half at the polarizing beam splitter. Different settings applied to WP2 and the corresponding results further confirm our theoretical analysis of the generation of the photonic state and its behaviour with respect to its polarization in the setup. This allow us to advance with new predictions of the outcome of the correlation measurements with variety of configurations for the polarizers in front of the SPAPDs presented in the following section.

4.3 Experiments and Results

As stated previously, we start experiments by setting both waveplates at the inputs of the PBS to 22.5° and two polarizers in front of the light-coupled multi-mode fibers leading to the SPAPDs. The experiments are initialized with a count rate registered by the SPAPD coupled to the B mode at 300 000 single photon counts per second whereas 15 000 counts are caused by leaked laser light from the cavity and the background noise in the laboratory interior.

We break this section into two parts − one where we leave the third half-waveplate (WP3) out of our setup and one where we install it before the non-polarizing beam splitter with angle set to 22.5°. Each part of this section will show four $g^{(2)}$-measurements with the polarizers A and B set to V-V, V-H, H-V and H-H, respectively. This adds up to eight total mea-

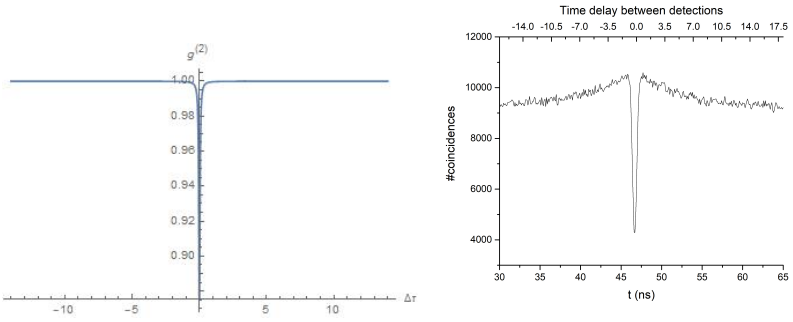

(a) ***(b)***

Figure 4.3: *V-V measurement in simulation (a) and the experimental result (b).*

surements. Each measurement was performed over a time period of 3000s.

Unfortunately, we were unable to manage the coherent pulsed laser to be in resonance with the quantum dots resulting in poor single photon counts. Due to the lack of time for the project, we proceeded to perform our measurements only with single photons produced by a continuous-wave laser. The CW correlation measurements produce significantly different results to what the pulsed case would yield. The main difference is that the pulsed laser would produce peaks at points of time delays between coinciding photons while the CW-laser forms dips at points where coincidences do not take place. Therefore, a coincidence with larger time delay than 3.5 ns between the photons contributes to the depth of several dips at once while the pulsed laser coincidences always contribute to only one peak at a time.

Alongside our experimental results, we will also present our predictions simulated based on the rules and results presented in chapter 3 and compare them to the measurements. These predictions give us $g^{(2)}$-prediction results where x-axis indicates time difference between the detections and y-axis corresponds to the probabilities of the dips emerging at a specific points of time delay.

4.3.1 Experiments without WP3

V-V

We begin by setting both polarizers to V-polarization. Our predictions (Fig. 4.3a) state that we should observe only one dip in the correlation measurement. This one dip emerges due to the fact that the detected V-polarized photons are all reflected off the PBS while everything that is

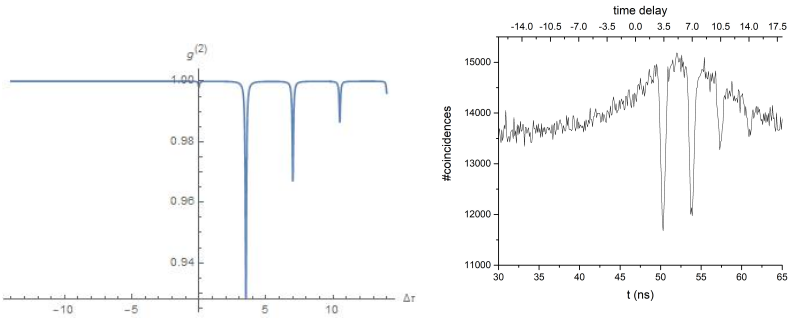

(a) ***(b)***

Figure 4.4: *V-H measurement in simulation (a) and the experimental result (b).*

transmitted out of the loop must be of H-polarization. Therefore, we detect only a stream of single photons with random intervals.

Our experimental data (Fig 4.3b) agrees with our predictions by producing a dip with over 50% dip depth. This result displays not only sufficiently high single photon flow from our photon source but also the location of the zero time delay $\tau = 0$ between the photons on our plot where the data was registered over continuous time due to path length differences in both output modes of non-polarizing BS, the multi-mode fibers as well as electronic cables. From the data we determined the zero time delay point to correspond to 46.9 ns on the lower x-axis.

We also observe a broad peak which emerges around the dip in our experimental data. We suspect this broad peak to be a result of spectral diffusion in our single photon source [28] and it must be inspected in the future. This emerging broad peak will be observable in all the experimental data, as will be shown in this section.

V-H

In order to predict photon correlations for the V-H case (Fig. 4.4a), we need to write out our photonic state in our setup at time of 7 ns corresponding to equation (3.14)

$$
\begin{aligned}
|\Psi\rangle = \frac{1}{2\sqrt{2}}|VH\rangle_{0,7} + \frac{1}{2\sqrt{2}}|VV_l\rangle_{0,7} + \frac{1}{2}|VV_l\rangle_{0,3.5} \\
+\frac{1}{2\sqrt{2}}\Big(|H\rangle_{3.5}\frac{1}{\sqrt{2}}\Big(|H\rangle_7 + |V_l\rangle_7\Big) + |V\rangle_{3.5}\frac{1}{\sqrt{2}}\Big(|H\rangle_7 - |V_l\rangle_7\Big)\Big) \\
+\frac{1}{2\sqrt{2}}|HV\rangle_{3.5,3.5} + \frac{1}{4}\Big(|HH\rangle_{7,7} - |V_lV_l\rangle_{7,7}\Big). \qquad (4.1)
\end{aligned}
$$

where photons are outside of the loop unless indicated with the lower index l which means that they enter the loop at the assigned to them time.

The state indicates that out of all possible events where there are one V- and one H-polarized photon, the V-polarized photon arrives at the detectors first, triggering input detector first. This results in the dips appearing only on the right hand side of $\tau = 0$.

The absence of the dip at $\tau = 0$ is explained by the continuous chain of photons flowing into the setup. Every time a photon goes into the loop instead of being reflected off of the PBS, there is a gap in that chain. When the photon is transmitted out of the loop 3.5 ns later, it is detected simultaneously with a new V-polarized photon which is part of the in-going chain. This reduces the dip at $\tau = 0$ due to the normalization of the state. This is visible in the term $\frac{1}{2\sqrt{2}} |HV\rangle_{3.5,3.5}$. However, since the probabilities of each detection event correspond to the depth of the dips, the state $|\Psi\rangle$ must be evolved much further in time in order to display that the probabilities of two photons arriving at the detectors simultaneously cancel out factors corresponding to the increase in depth of the dip at $\tau = 0$.

The exponential drop in height of the dips, the further they are from the point $\tau = 0$, is due to the fact that the probability of a photon coming out of the loop drops by half at every round it stays inside the loop.

Experimental data (Fig. 4.4b) displays a clear absence of the dip at $\Delta\tau = 0$. However, the data does not show the exponential drop in depth between the dips at $\tau = 3.5$ ns and $\tau = 7$ ns. Rather, they appear nearly equal in depth which implies that we have an increasing factor of the probability of detections with relative time delay of 3.5 ns. Dips following after $\tau = 7$ ns proceed to decrease exponentially.

H-V

Predictions (Fig. 4.5a) indicate that by swapping the polarizations between Pol A and Pol B, the dips in the correlation measurement should appear now on the left side of the point at $\tau = 0$ as opposed to outcome in the V-H measurement. They should, however, decrease exponentially with the absence of the dip at $\tau = 0$. I.e., there should be a symmetry between V-H and H-V measurements with respect to the y-axis at $\tau = 0$. The reason for the dips appearing on the other side is simply because the sync port detects a photon this time first.

Now, the experimental data (Fig. 4.5b) displays discrepancies to our predictions by two identical-in-depth dips. This time dip at $\tau = -7$ and $\tau = -10.5$ ns. Additionally, the dip at $\tau = -7$ is not of half the depth of the dip at $\tau = -3.5$. This breaks the hypothesized symmetry conservation

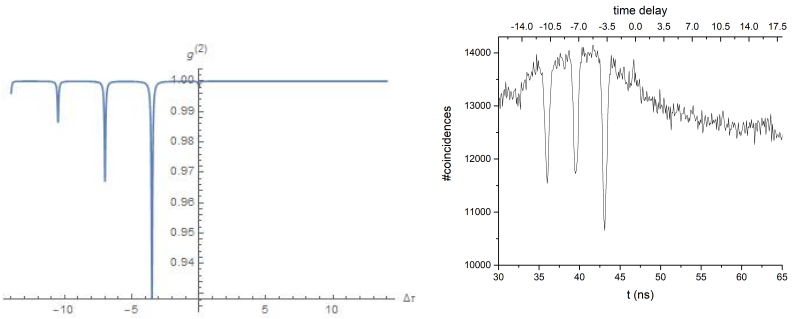

(a) **(b)**

Figure 4.5: *H-V measurement in simulation (a) and the experimental result (b).*

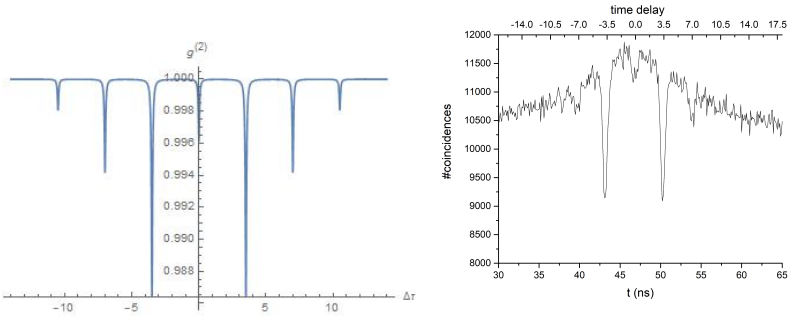

(a) **(b)**

Figure 4.6: *H-H measurement in simulation (a) and the experimental result (b).*

from V-H measurement. From the comparison with the data of V-H measurement, the depth of the dip at $\tau = 3.5$ ns of V-H data is equal to the depth of $\tau = -3.5$ ns in H-V data, ruling out the variation in the events corresponding to these dips between the two measurement data. This indicates that the change happens (in comparison to V-H) in $\tau = -7$ and $\tau = -10.5$ ns. The smaller dip at $\tau = -7$ and larger dip at $\tau = -10.5$ ns show increased number of coincidences with time delay of 3.5 ns.

H-H

Simulation result (Fig. 4.6a) shows a reduced dip at $\tau = 0$ due to the photobunching emerging at WP2 caused by the HOM-effect which is presented in the last two terms of the photonic state in equation (4.1). The HOM-effect plays a role only in this detection configuration as two H-polarized photons can come out of the loop simultaneously reducing the size of the zero dip. The simulation data, additionally, tells us that the

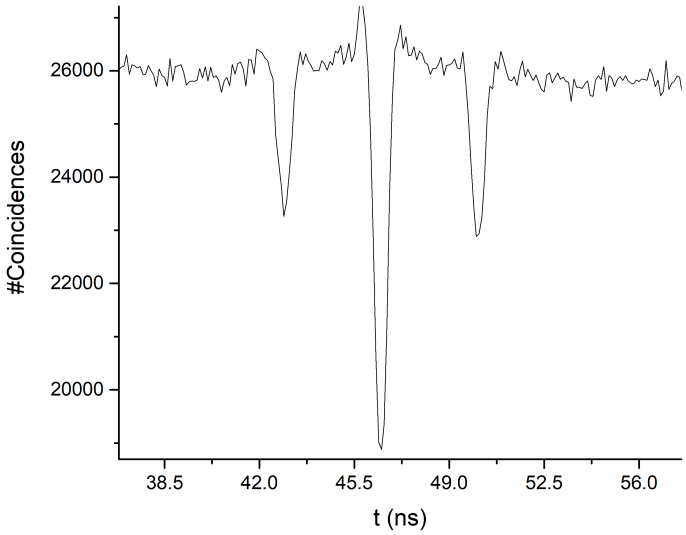

Figure 4.7: *H-H experimental result without HOM-effect taking place at WP2.*

ratio between dips at -3.5, -7 and 3.5, 7 is 7:3, respectively while the ratio between -7, -10.5, and 7, 10.5 is 2:1.

Experimental data (Fig. 4.6b) shows a small observable dip at the zero point which seems to agree with the simulation data in terms of ratios between this and the neighbouring dips. This dip should indeed be present due to two photons that can be stuck in the loop indefinitely which is shown in the last term of the equation (4.1). Due to the noise in the data and the increase in the photon counts, it is hard to determine the ratios between the dips.

If the HOM-effect did not take place in the loop, it would mean that the loop is slightly misaligned and the photons wouldn't arrive at WP2 simultaneously resulting in continuous chain of single H-polarized photons coming out of the loop. This would turn out as an increased dip at $\tau = 0$ which we observed in an experimental data in Figure 4.7 obtained in early stages of our experiments. This served for us as an indication that the loop was not aligned.

Discussion

Despite of the discrepancies emerging in V-H and H-V measurements, the experimental data seems to mostly agree with predicted theory which was

a further indication that our theory about the generated photonic states in the setup is, in fact, correct.

However, the symmetry breaking between V-H and H-V data is a reason for concern. Misalignment of the loop is most likely not the reason for such discrepancies as the symmetry in H-H and V-V results was preserved. This may suggest that there may be a faulty optical element in one of the modes between the non-polarizing beam splitter and the polarizers which influences one of the two polarizations. This would explain why we witness symmetry breaking in only V-H and H-V measurements. This must be investigated in the future to determine and quantify the effect of imperfections.

An interesting aspect arising in the experimental data is the distinct increase in photon counts around the delay points in time where the dips were formed. Interestingly, this increase would shift from one place in time to another depending on the quantity of dips. This is observable in V-H and H-V measurement data. In V-H data the highest photon count is recorded at $\tau = 5.2$ ns while in H-V measurement the location shifts to $\tau = -5.2$ ns. In addition, the location seems to be influenced by the amount of depth of the dips as the highest count always appears precisely in between two deepest dips which can be seen also in V-V as well as H-H measurement data. The increase is most likely caused by the spectral diffusion in the single photon emission in the quantum dot [28]. However, this issue needs further inspection in the future.

Additional imperfection effects that can influence the presented scheme must be brought up. The photons from the source may not be in a pure state due to imperfect degree of polarization [3]. The source may also create slightly distinguishable photons reducing the affect of HOM-effect on the outcome. The background noise from the laser and other external light sources in the laboratory environment can also cause disruptions. Slight asymmetric aspects in the setup such as imperfect alignment may affect the results as well. All the effects of imperfections should, therefore, be quantified in the future in order to make predictions more accurately as the current predictions were based on the ideal cases with perfect alignment, degree of polarization and pure state.

Finally, we look at the photons in the second row of the state in equation (4.1). If the photon pairs were indeed entangled, then the photon inside the loop $|D\rangle_7$ would correspond to $|H\rangle_7$ and come out of the loop to be detected 3.5 ns after the first H-polarized photon while $|A\rangle_7$ would correspond to $|V\rangle_7$ and remain inside the loop and be possibly detected 7 ns after the first detected V-polarized photon [3]. This would be a reducing factor in dips at $\tau = -3,5$ and 3.5 ns in H-H measurements and $\tau = -7$

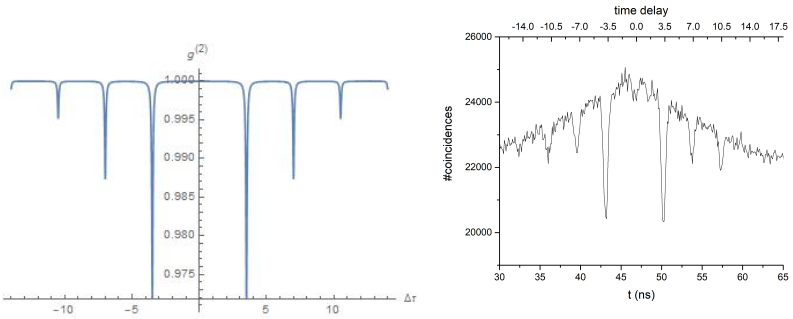

(a) ***(b)***

Figure 4.8: *V-V measurement with WP3 in simulation (a) and the experimental result (b).*

and $\tau = 7$ in H-V and V-H measurements, respectively. However, we see the opposite behaviour in the latter two measurements where dips at -7 and 7 appear to be much deeper than predicted. As of this moment it is unclear why we observe such behaviour. Nonetheless, this does not rule out that the entanglement can be present between the photons. Further analysis must be performed after quantification of the possible imperfections mentioned above. Another important step would be a performance of quantum state tomography which could give a direction in understanding the discrepancies in our data and the elements which cause them. The pure state of two qubits may be decomposed into a superposition of a maximally entangled state and orthogonal separable state [9] and therefore quantum tomography would also provide more insight in the degree of entanglement of our state.

4.3.2 Experiments with WP3

The following experiments were performed after installing additional half-waveplate in the input mode of the non-polarizing beam splitter. Due to the rotated polarization basis, we now have to consider every possible event coming from the PBS for set configurations of the polarizers.

V-V

The main difference between the measurements without WP3 is that now the bunched photons from the HOM-effect at WP2 become detectable. The simulation in Figure 4.8a therefore displays the absence of the dip in the zero point. Additionally, the term $\frac{1}{2\sqrt{2}} |HV\rangle_{3.5,3.5}$ in equation (4.1) also

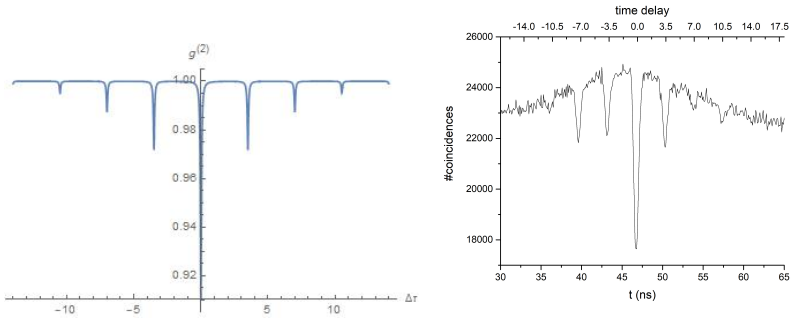

(a) ***(b)***

Figure 4.9: *V-H measurement with WP3 in simulation (a) and the experimental result (b).*

results in HOM-effect with bunched photon pairs at WP3. This explains why the dip is completely absent unlike in the simulation of H-H without WP3 (Fig 4.6a).

The experimental data (Fig. 4.8b) seems to largely agree to the result of the simulation. The tiny dip at the zero point is most likely again due to the photon pair stuck inside the loop, indefinitely. Somewhat striking difference to the simulation data is that the dips at $\tau = -7$ and $\tau = 7$ ns appear to be of equal size to the dips at $\tau = -10.5$ and $\tau = 10.5$ ns.

V-H

Simulation (Fig. 4.9a) now displays that HOM-effect creates a dip at the zero point unlike in V-V measurement where it reduces it. The quantum interference at WP3 turns the photons in the term $\frac{1}{2\sqrt{2}} |HV\rangle_{3.5,3.5}$ into a pair of H-polarized photons or V-polarized photons reducing greatly the detection of events detected at the same time resulting in the greater dip at zero delay point. Additionally, dips now appear on both sides as rotated V-polarized photons can now correspond to H polarization. The dips around the zero point would obey the symmetry. Beyond the points $\tau = -3.5$ and $\tau = 3.5$, the dip depths drop exponentially in periods of 3.5 ns.

Experimental data (Fig. 4.9b) agrees on the dip emerging at zero point after the addition of the waveplate and dips appearing on both sides of the zero point. However, the symmetrical aspect of the data is broken. Dips at -7 and -3.5 ns appear to be equal in depth while dip at 7 ns is extremely shallow in comparison to the dip at 3.5 ns. However, dips of 3.5 and -3.5 ns are of the same depth. This could potentially suggest that the element

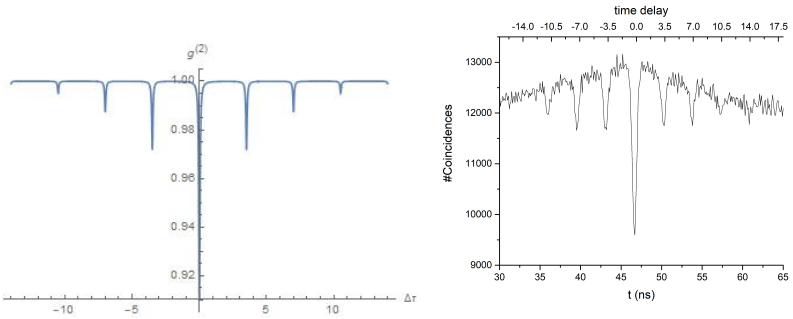

(a) ***(b)***

Figure 4.10: *H-V measurement with WP3 in simulation (a) and the experimental result (b).*

of imperfection affecting only one of the polarizations is located in mode A of the BS and it influences specifically V-polarized light. However, this does not explain why the dip at 3.5 ns, then, appears to be unaffected by this element.

H-V

Figure 4.10a tells that the simulation predicts identical outcome to the result of the simulation of V-H configuration.

The experimental (Fig. 4.10b) data mostly agrees with the predictions. Despite the drop in total photon count in the experiment, the ratio between the dips around the zero point and the zero dip is precisely the same as in the V-H experimental data. However, this time the dip does not disappear at -7 nor 7 ns which further suggest that the mode A might have some influence on V polarization. Symmetry, therefore, is preserved just as predicted in the simulation data. However, the dips at -7, -3.5, 3.5, and 7 ns, all appear to be of the equal depth.

H-H

The simulation data in 4.11a tells us that the outcome must be identical to V-V experiment. The rotation of the polarization bases at WP3 should indeed create HH and VV polarized photon pairs with equal probabilities regardless of the polarization of the photons coming from the PBS. The zero dip must be absent due to the HOM-effect at both, WP2 and WP3.

In this experimental data (Fig. 4.11b), we observe rather surprising feature. Dips at -3.5 and 3.5 ns are nearly indistinguishable while zero dip is

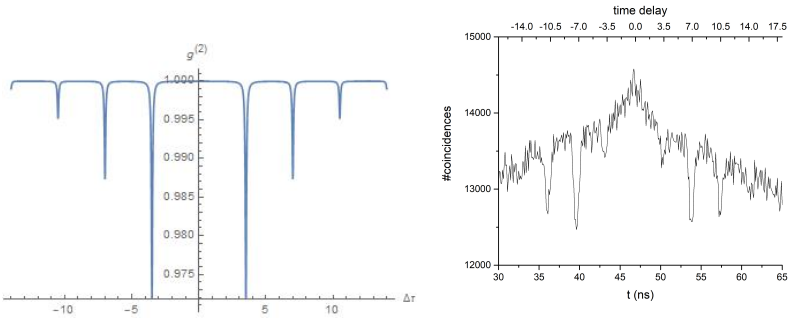

(a) ***(b)***

Figure 4.11: *H-H measurement with WP3 in simulation (a) and the experimental result (b).*

completely absent. This means that some element in the setup is causing an increase in the number of photon pairs arriving with time difference of 3.5 ns while increasing the absence of coincidences with higher time differences. We did not observe such critical discrepancies in any other measurement data which further suggests that the elements of imperfections are after the non-polarizing beam splitter. One possible explanation of this could be a slight misalignment in the loop increasing the number of photons detected after one round inside the loop while decreasing detected number of photons that stayed in the loop more than one round. This is possible if after the second round in the loop, the light is in worse alignment with the reflected photons going in the direction of the non-polarizing BS. However, this type of discrepancies were not observed in any other experimental data which makes the misalignment of the loop an unlikely major element of imperfection. Apart from the misalignment of the loop, as of the moment of writing of this thesis, we have no relevant explanation for this anomaly.

Discussion

We need to keep in mind that since the possible elements of imperfection were not included in the simulations, it is not fully accurate to compare the results of both experimental and simulation data. However, it can give us a direction for our attention into the locations of the major influencing elements in our setup. Additionally, despite the discrepancies in the comparisons, we can extract information concerning emerging entanglement in the generated cluster states.

The presence of the entanglement and its effect on the outcome in the

four measurements with WP3 discussed in this section can be observed with inspection of the ratios between the depths of the dips. Mainly in V-H and H-V measurements. According to our prediction simulations if the entanglement features are removed, the ratio between the zero dip and other dips around it changes significantly while the ratios between the dips that exclude the zero point remains the same. Therefore, the data of V-V and H-H measurements can not provide us with any information on the existence of the entanglement as the zero dip is absent in both of them.

In future, we may be able to prove the generation of the entangled cluster states within the setup. This would require the further calculations of the ratios between the dips in the experimental data and fitting it to the predicting simulations. This would enable us to create one or several quantum witnesses [29] based on these observations.

Another possibility to confirm the detection of the entaglement in our photonic state would be the construction of an entanglement witness [9] based on the density matrix form of the photonic state obtained with quantum state tomography. It is a functional which segregates entangled state from separable ones in a quantum state. However, performing the quantum state tomography is not an easy task for as complicated photonic states as ours.

Chapter 5

Conclusion

In conclusion, with tunable continuous-wave excitation laser, we have successfully generated single photon stream into the setup with the delay loop.

Furthermore, the characterization of two-photon states has produced robust similarities between the simulated results and experimental data in $g^{(2)}$-measurements with different post-selecting polarization configurations in two different polarization bases. This shows us that the loop setup, works according to our theory which we produced in chapter 3 and that the cluster states were generated in the setup. In addition, we observed photobunching in our experimental data in V-V and H-H measurements as a product of the HOM-effect at the waveplate inside the loop. This further proved that not only was the loop aligned properly but also that the photons were, indeed, indistinguishable from one another.

Nonetheless, relatively small discrepancies between predictions and experimental data were observed. This is due to the fact that the state and the environment of the setup were considered to be ideal without the elements of imperfection influencing the photonic state during the generation process over time in the simulations. These imperfections are mainly impurity of the state, not complete indistinguishability between photons and misalignment of optical elements of the setup. These imperfections can be quantified to further improve the comparison.

The evidence of the entanglement in the setup can be drawn from the information about the ratios between the depths of the dips in the experimental data. Our simulations show that if the entanglement and the quantum interference are removed from the setup, the ratios of the dip depths would change between the zero time delay dip and the dips at other time delays. This can be seen in V-H and H-V measurements with the third

half-waveplate. If the elements of the impurities are quantified and we determine the ratios between the dips when the entanglement is present, we can run a more accurate comparison between the simulations and the experimental data. Based on these ratios, we can construct an entanglement witness and deduce that our photons are indeed entangled.

In the future, the quantum state tomography can be performed to provide us with more insight into the photonic state in the form of a density matrix. This will provide us with further information on characterization of the entanglement and its degree. Perhaps, even new ways of isolating presumably entangled photon pairs can be found which would make the direct measurement of correlations between them in two different polarization bases possible.

If the success is found in detecting entanglement in cluster states with two photons, we are hopeful to move onto experiments for the quantum states with higher number of photons in the future.

Bibliography

[1] Feynman, R. P., Leighton, R. B., & Sands, M., The Feynman Lecture on Physics, Volume III, *The California Institute of Technology* (1965).

[2] Akama, S., Elements of Quantum Computing: History, Theories and Engineering Applications, *Springer* (2014).

[3] Pilniyak, Y., Aharon, N., Istrati, D., Megidish, E., Retzker, A., & Eisenberg, H. S., Simple source for large linear cluster photonic states, *Phys. Rev. A.* **95** 2 (2016).

[4] Nielsen, M. A., Optical Quantum Computation Using Cluster States, *Phys. Rev. Lett.* **93** (2004).

[5] Raussendorf, R,. & Briegel, H. J., Quantum computing via measurements only, *LMU München* 1-4 (2018).

[6] Cirac, J. I., & Zoller, P., A scalable quantum computerwith ions in an array of microtraps, *Nature* **404**, 579-581 (2000).

[7] Xing-Cao, Y., Tian-Xiong, W., Ping, X., He, L., Ge-Sheng, P., Xiao-Hui, B., Cheng-Zhi, Peng., Chao-Yang, L., Yu-Ao, C., & Jian-Wei, P., Observation of eight-photon entanglement, *Nature Photonics,* **6** 225-228 (2011).

[8] Heinosaari, T., & Ziman, M., Mathematical Language of Quantum Theory, From Uncertainty to Entanglement, *Cambridge University Press* (2011).

[9] Gühne, O., & Toth, G., Entanglement detection, *Phys. Rep.* **474**, 1-75 (2009).

[10] Peres, A., Separability Criterion for Density Matrices, *Phys. Rev. Lett.* **77** 1413-1415 (1996).

[11] Simon, R., Peres-Horodecki separability criterion for continuous variable systems, 9909044, 1-6 (1999).

[12] Zyczkowski, K., Horodecki, P., Sanpera, A., & Lewenstein, M., On the volume of the set of mixed entangled states, *Phys. Rev. A.* **60** 3496-3507 (1998).

[13] Dür, W., Vidal, G., & Cirac, J. I., Three qubits can be entangled in two inequivalent ways, *Phys. Rev. A.* **62** 062314-062311 (2000).

[14] Acin, A., Adrianov, A., Costa, L., Jane, E., Larotte, J. I., & Tarrach, R., Generalized Schmidt decomposition and classification of three-quantum-bit states, *Phys. Rev. Lett.* **85** 1560-1563 (2000).

[15] Snijders, H., Frey, J. A., Norman, J., Post, V. P., Gossard, A. C., Bowers, J. E., van Exter, M. P., Löffler, W., & Bouwmeester, D., Fiber-Coupled Cavity-QED Source of Identical Single Photons, *Phys. Rev.* 031002 (2018).

[16] Snijders, H., Frey, J. A., Norman, J., Post, V. P., Gossard, A. C., Bowers, J. E., van Exter, M. P., Löffler, W., & Bouwmeester, D., Supplemental: A fiber-coupled cavity-QED source of identical single photons, *Leiden University* (2018).

[17] Fattal, D., Single Photons for Quantum Information Processing, PhD Thesis, *Stanford University* (2010).

[18] Fox, M. S., Quantum Optics: An Introduction, *Oxford Master Series in Physics* (2006).

[19] Walther, P., Resch, K. J., Rudolph, T., Schneck, E., Weinfurter, H., Vedral, V., Aspelmeyer, M., & Zeilinger, A., Experimental one-way quantum computing, *Nature*, **434** 169-176 (2005).

[20] Briegel, H. J., & Raussendorf, R., Persistent entanglement in arrays of interacting particles, *Phys. Rev. Lett.* **86** 910-913 (2001).

[21] Ornes, S., Core Concept: Quantum dots, *Proceedings of the National Academy of Sciences*, **113** 2796-2797 (2016).

[22] Bakker, M., Cavity quantum electrodynamics with quantum dots in microcavities, PhD Thesis, *Leiden University* (2015).

[23] Hennessy, K., Badolato, A., Winger, M., Gerace, D., Atatüre, M., Gulde, S., Fält, S., Hu, E. L., & Imamoglu, A., Quantum nature of a strongly coupled single quantum dot cavity system, Nature **445**, 896-899 (2007).

[24] Anshou, Z., Guangyong, Z., Hongyun, C., Tingting, M., & Jibing, L., Nonreciprocal light propagation in coupled microcavities system beyond weak-excitation approximation, *Scientific Reports*, **7** 1-9 (2017).

[25] Shore, B. W., Topical Review: Jaynes Cummings Model, *Journal Of Modern Optics* **40**, 1195-1238 (1993).

[26] ARC Electronics, FiberOptic Cable Tutorial, *ARC Electronics*, **25** 301-924-7400 (2007).

[27] LabView^{TM} LabView software 2018, (2018).

[28] Kang, G., Solovev, I., Holmes, M., Arita, M., & Arakawa, Y., Nanosecond-scale spectral diffusion in the single photon emission of a GaN quantum dot, *AIP Advances*, **7** 0-5 (2017).

[29] Jain, R., Kerenidis, I., Kuperberg, G., Santha, M., Sattath, Or., & Zhang, S., On the power of a unique quantum witness, *Main*, 1-17 (2009).